Ground Clutter and Noise Mitigation Based on Range–Doppler Spectral Processing for Polarimetric Weather Radar

Mengyun An, Jiapeng Yin, Jiankai Huang, Xue Tan, and Yongzhen Li

***Abstract*—Spectral polarization filtering in the range–Doppler domain plays an important role in weather radar clutter mitigation. However, when ground clutter and precipitation overlap, these methods tend to filter out clutter-contaminated precipitation, leading to estimation errors. To address this problem, this article proposes a ground clutter and noise mitigation method based on range–Doppler spectral processing for polarimetric Doppler weather radars. The proposed method can filter out clutter and noise and retain precipitation overlapped with clutter by analyzing the property differences between precipitation and clutter and noise in the range–Doppler spectrogram. Specifically, due to the spatial continuity of precipitation in the range–Doppler domain, the spectral moments (e.g., velocity and spectral width) are also continuous. In addition, polynomial fitting is used to compensate for the missing spectral moments, and the missing precipitation is recovered by Gaussian fitting using the computed spectral moments. The results demonstrate performance improvements after applying the proposed method to radar data collected by Chinese operational weather radars. The proposed method is compared with several other algorithms, and the comparison results show that the proposed method performs best in clutter and noise suppression and precipitation retention performance.**

***Index Terms*—Clutter mitigation, polarimetric Doppler weather radar, precipitation retention, spectral continuity, spectral moment.**

I. Introduction

POLARIMETRIC Doppler weather radars acquire hydrometeorological data from weather observations with high spatial and temporal resolution [1]. These data are crucial for quantitative precipitation estimation [1], [2], [3], [4], classification, short-term weather forecasting [5], and subsequent warning operations [6]. The prerequisite of using weather radar data is achieving sufficient measurement accuracy. However, the quality of weather radar measurements is highly susceptible to clutter [7], such as ground clutter (GC), sea clutter, biological echoes, wind turbine clutter, and radio frequency interference [7]. The extraction of useful data can be severely restricted by clutter.

According to the Doppler velocity, weather radar clutter can be divided into stationary clutter and nonstationary clutter [8], [9], and the stationary clutter usually refers to GC. Traditionally, a static clutter map constructed under clear-air conditions is typically used to locate gates contaminated by GC [9]. However, the clutter map can change depending on meteorological conditions due to anomalous electromagnetic wave propagation [10]. In addition, GC is not entirely stationary, and vegetation flutter and power lines swing can effectively widen the clutter spectrum by generating extended tails [11]. Thus, a robust GC detection algorithm is necessary before filtering.

The clutter mitigation decision (CMD) algorithm based on a fuzzy logic method [12], [13] has been the most widely used GC detection algorithm in recent years [14], [15], [16]. However, this algorithm returns false detection along zero isodops. To improve the clutter detection performance, the spectral properties have been considered in [14] and [15], and the spectrum clutter identification (SCI) algorithm was introduced based on a simple Bayesian classifier; still, this algorithm requires large computational resources. Both of the aforementioned methods include more than three parameters that can increase computation complexity. More recently, the phase fluctuation index was introduced to discriminate clutter from weather signals [16], [17]. Considering the difference in correlation time between precipitation and GC, the dual-scan (DS) approach was developed in [18] to improve the clutter detection performance. Furthermore, to use the polarization properties fully, Li et al. [19] presented the dual-polarization (DP) clutter detection algorithm based on the power ratio, the cross-correlation coefficient ρ_{hv}, and the differential reflectivity Z_{dr}. Taking full advantage of differences in correlation time and polarization, Golbon-Haghighi et al. [20] developed the DPDS algorithm that combines the DP with the DS and can efficiently perform classification [18]. However, the DS and DPDS methods require the I&Q data [I&Q refers to the in-phase (I) and quadrature (Q) components of a complex signal] from two scans, which cannot meet the real-time requirement. In addition, Nan et al. [21] identified the GC combining fuzzy logic classification and statistics on the spatial distribution of reflectivity. However, it can be challenging to identify the AP

Manuscript received 30 January 2024; revised 9 April 2024 and 5 June 2024; accepted 24 June 2024. Date of publication 1 July 2024; date of current version 8 July 2024. This work was supported in part by the National Natural Science Foundation of China under Grant 61921001 and Grant 61971429, and in part by the Postgraduate Scientific Research Innovation Project of Hunan Province under Grant QL20220011. *(Corresponding author: Jiapeng Yin.)*

Mengyun An, Jiapeng Yin, Jiankai Huang, and Yongzhen Li are with the State Key Laboratory of Complex Electromagnetic Environment Effects on Electronics and Information System and the College of Electronic Science, National University of Defense Technology, Changsha 410073, China (e-mail: anmengyun20@nudt.edu.cn; jiapeng.yin@hotmail.com; huangjiankai08@163.com; Liyongzhen@nudt.edu.cn).

Xue Tan is with the Chengdu Jinjiang Information Industry, China Electronics Corporation (CEC), Chengdu 610011, China (e-mail: tanx000@163.com).

Digital Object Identifier 10.1109/JSTARS.2024.3420074

clutter because it is likely to be nonstationary within the statistical period [21]. Moreover, if only these recognition algorithms are used for GC suppression, precipitation might be removed when GC is embedded in precipitation.

In recent years, with the introduction of spectral polarimetric techniques, tremendous progress has been achieved in the fields of artificial target characterization in polarimetric synthetic aperture radar [22], [23] and clutter mitigation for weather radar. The double spectral linear depolarization ratio (DsLDR) filter applied to the range–Doppler (RD) spectrogram [i.e., the azimuth of plan position indicator (PPI)] was proposed by Unal [24]. To maintain the continuity of precipitation and suppress the narrow band clutter, the moving DsLDR (MDsLDR) filter was proposed in [25]. The MDsLDR filter can be used only in fully polarimetric weather radars with cross-polarization measurement capabilities. However, operational weather radars do not always possess full polarimetric measurement. Therefore, Yin et al. [8] put forward the object-orientated spectral polarimetric (OBSpol) filter and the moving spectral depolarization ratio (MsDR) filter [26] for clutter and noise suppression in DP weather radars without cross-polar measurements. Nevertheless, these spectral polarimetric methods tend to filter out the clutter-contaminated precipitation, which can lead to precipitation discontinuities in areas overlapping with GC.

The aforementioned methods effectively detect and remove clutter but do not consider situations where clutter and precipitation coexist simultaneously. To address this problem, the Gaussian model adaptive processing (GMAP) was proposed in [27]. This method requires an enormous computing volume and a lengthy calculation period since the moments are repeatedly computed, and the gap is repeatedly filled until reasonable convergence [27], [28]. Furthermore, prior to using the GMAP approach, the GC locations need to be identified. To integrate detection and filtering into one algorithm, the clutter environment analysis using adaptive processing (CLEAN-AP) was proposed in [29]. The CLEAN-AP uses the phase of coefficients in the autocorrelation spectral density to suppress GC and reduce bias in weather target estimation. Hubbert et al. [30] introduced a time-domain regression filter approach, but this approach was not validated by real measurement data. To solve the loss of zero-velocity precipitation, Yin et al. [31] developed the kriging algorithm, which is computationally intensive and, thus, not suitable for real-time weather radar. Moreover, an RD regression (RDR) algorithm was proposed to recover precipitation contaminated by wind turbine clutter. The limitation of this method is that it requires knowledge of the contaminated range gates' location [32].

This article proposes a GC and noise mitigation method for polarimetric Doppler weather radars that can suppress GC and noise and retain precipitation when these echoes overlap. Compared with the GMAP, which constantly adjusts the type and size of the window to recompute the moments and refill the gap, the proposed method can exploit the spatial continuity of precipitation to compensate for the missing spectral moment. The gap is rapidly filled by a Gaussian function defined using the computed spectral moments without too much iteration.

The rest of this article is organized as follows. The spectral polarimetric observables and the clutter characteristics are introduced in Section II. In Section III, the proposed clutter and noise suppression approach is described in detail. The parameter selection and the performance of the proposed approach are compared with those of the OBSpol filter, MsDR filter, and the method combining CMD with GMAP in Section IV. In Section V, the robustness of the proposed method is validated using radar data collected in Guangzhou, China. Finally, Section VI concludes this article.

II. Weather Radar Observation

A. Spectral Polarimetric Observables

Spectral polarimetric technology, combining Doppler and polarization information, is helpful in retrieving precipitation microphysical information and mitigating nonhydrometeor echoes [8], [24].

Following the backscatter alignment convention, the spectral reflectivity, which relates to the range r and Doppler velocity v, can be expressed as follows [24]:

$$sZ_{xy}(r,v) = C \cdot sP_{xy}(r,v) \cdot r^2 = C \cdot |sS_{xy}(r,v)|^2 \cdot r^2 \quad (1)$$

where $sS_{xy}(r,v)$ is the complex Doppler velocity spectrum, with a transmitted x polarization and a received y polarization, where x and y stand for horizontal (i.e., h) and/or vertical (i.e., v) polarization, respectively; $sP_{xy}(r,v)$ is spectral power; C represents radar calibration constant.

Then, the definition of the spectral differential and the spectral copolar correlation coefficient $s\rho_{\text{co}}(r,v)$ [24] can be, respectively, expressed by

$$sZ_{\text{dr}}(r,v) = 10\log_{10}\left(\frac{sZ_{\text{hh}}(r,v)}{sZ_{\text{vv}}(r,v)}\right) \quad (2)$$

$$s\rho_{\text{co}}(r,v) = \frac{|\langle sS_{\text{hh}}(r,v) \cdot sS^*_{\text{vv}}(r,v)\rangle|}{\sqrt{\left\langle |sS_{\text{hh}}(r,v)|^2 \right\rangle \left\langle |sS_{\text{vv}}(r,v)|^2 \right\rangle}} \quad (3)$$

where $\langle\rangle$ represents the sample average in Doppler, and the running average consists of three consecutive Doppler bins [8]; $s\rho_{\text{co}}$ describes the correlation between $sS_{\text{hh}}(r,v)$ and $sS_{\text{vv}}(r,v)$ and plays a significant role in clutter mitigation; however, $s\rho_{\text{co}}$ is not sufficient for GC suppression due to the $s\rho_{\text{co}}$ distribution overlapped between precipitation and GC [26], [33].

In this study, the clutter phase alignment (CPA) is used to identify GC, which represents a parameter of temporal phase fluctuations of a resolution cell [12]. The CPA is related to the velocity and spectrum width of a signal. This indicator has been shown to provide good discrimination between clutter and noise and weather signals [12], [13].

The CPA in a range r is expressed as follows:

$$\text{CPA(r)} = \left|\sum_{n=1}^{N} x_n(r)\right| \Big/ \left|\sum_{n=1}^{N} |x_n(r)|\right| \quad (4)$$

where $x_n(r) = I_n(r) + jQ_n(r)$ represents the complex radar-received time series in the range r with $j = \sqrt{-1}$; N is the number of samples in a dwell time.

The CPA values range from zero to one, where the value of one indicates a very high probability of clutter because the backscattering phase of the ground target is basically fixed, and

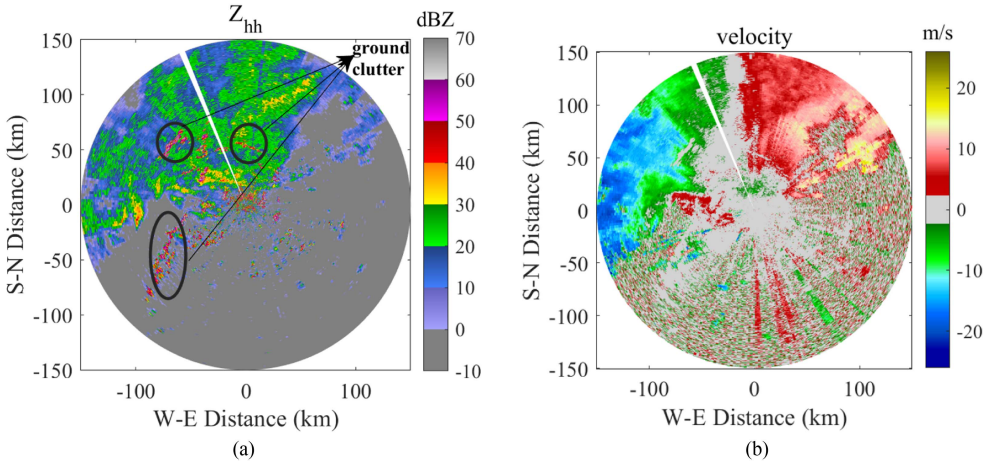

Fig. 1. Raw PPI observations of the Ji'an radar. Data were measured at 21:11 CST on March 5, 2021. (a) Raw Z_{hh} data. (b) Raw velocity data.

TABLE I
JI'AN RADAR SYSTEM SPECIFICATIONS

Radar type	Polarimetric Doppler
Polarization	STSR mode
Transmitted power (kW)	650
Wavelength (cm)	10.41
Range resolution (m)	300
Sample number	64
Scanning mode	VCP21
Scan angle (azimuth)	0 – 360°

the phase of the echo in time series is basically the same for specific azimuth and distance values [12], [13]. For distributed targets (e.g., precipitation), the phase varies among pulses with the target velocity and spectral width in the observation volume leading to a lower CPA value (mostly less than 0.5) for most nonzero-velocity weather echoes [12], [13]. The CPA is close to zero for noise due to its random behavior [12], [13].

Spectral polarimetric filters can retain precipitation and filter out clutter and noise, allowing for calculating standard moments and polarimetric observables. The reflectivity in range r is expressed by [1]

$$Z_{\text{hh}}(r) = C \cdot \sum_{v \in pre} (sP_{\text{hh}}(r, v) - sN) \cdot r^2 \tag{5}$$

where $v \in$ pre represents Doppler bins that contain precipitation; sN is the spectral noise for the selected spectrogram.

Reorganize RD spectrum power bins of sP_{hh} in ascending order of intensity. The average power in the range of 5%–40% is calculated. And the average is regarded as the estimated spectral noise [8], [27]. In addition, the radial velocity $\bar{v}$ and spectral width σ_v can be, respectively, obtained by [1], [24]

$$\bar{v}(r) = \frac{1}{Z_{\text{hh}}(r)} \sum_{v \in pre} v \cdot sZ_{\text{hh}}(r, v) \tag{6}$$

$$\sigma_v(r) = \sqrt{\frac{1}{Z_{\text{hh}}(r)} \sum\nolimits_{v \in pre} (v - \bar{v}(r))^2 \cdot sZ_{\text{hh}}(r, v)}. \tag{7}$$

These radar observables can be evaluated after applying the proposed method, as explained in Section IV.

B. Clutter Analysis

The specifications of Ji'an radar whose data are used in this study are given in Table I. The *S*-band polarimetric Doppler weather radar operating in the simultaneous transmission and simultaneous reception (STSR) mode is one of the National Weather Service Radars located in Ji'an, China.

The raw PPI observation data of Ji'an radar are shown in Fig. 1; these data were collected at a low elevation value of 0.5°. As shown in Fig. 1(a), there are points with a strong power due to the GC, which are indicated by the black circles. In Fig. 1(b), it can be seen that the velocity is discontinuous in the region where precipitation is located, as shown in the black circle. In addition, it can be noticed from the reflectivity and radial velocity that there is much GC close to the radar. The GC significantly impacts quantitative precipitation estimation, indicating the necessity for performing a GC suppression and employing a precipitation recovery algorithm.

For a closer look at the raw range-time image and RD spectrogram (i.e., one ray with 64 pulses in the radar PPI), Ray 193 is extracted, and the observables are shown in Fig. 2. According to Fig. 2(a) and 2(c), the power at 63 km is significantly higher than that at 30 km. Fig. 2(b) and 2(d) shows that although the main power is concentrated at zero velocity, the noise power at 63 km is significantly high. It can be concluded that this range bin is affected by GC, and the raised noise is caused by spectral leakage. Furthermore, to illustrate how GC affects precipitation, Ray 1 is extracted, and the spectral polarimetric observables are shown in Fig. 3.

In Figs. 2 and 3, the following characteristics of GC can be observed.

1) After applying the discrete Fourier transform (DFT) using a Hamming window, the GC main lobe concentrates around zero Doppler velocity.
2) Some GC spread out to the entire Doppler spectrum [e.g., 63 km in Fig. 2(b) and 2(d)].
3) The GC power of the two channels may not be equal [e.g., 63 km in Fig. 2(d), and 53 km in Fig. 3(c)].
4) When the power of GC is strong, both the main lobe energy and spectral leakage energy may be significant, leading

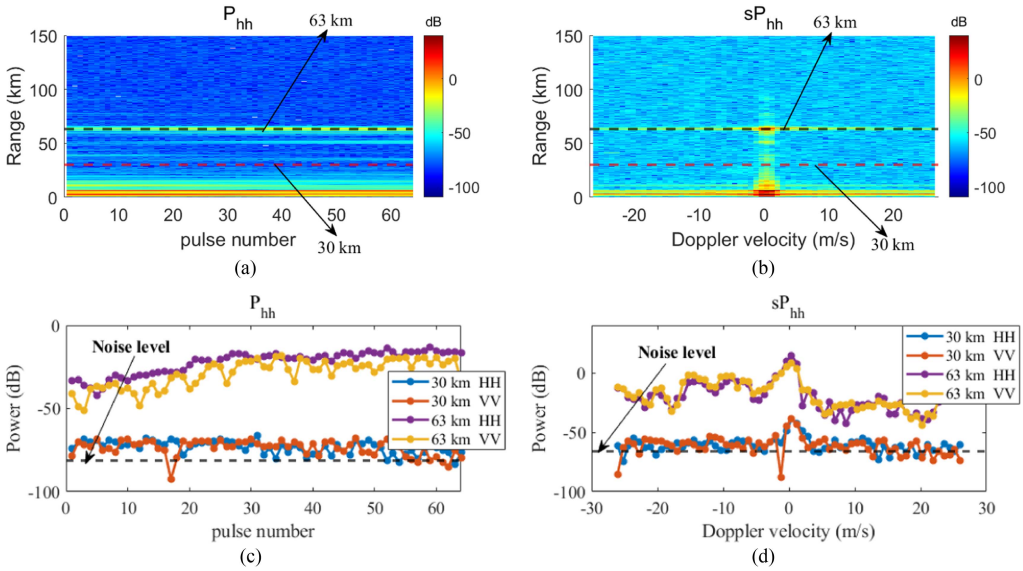

Fig. 2. Observables related to Ray 193 in Fig. 1. (a) Power P_{hh}. (b) Spectral power sP_{hh}. (c) Power of range bin 100 (30 km where there is no GC) and 210 (63 km where GC and its sidelobe exist). (d) Power spectrum of range bin 100 and 210.

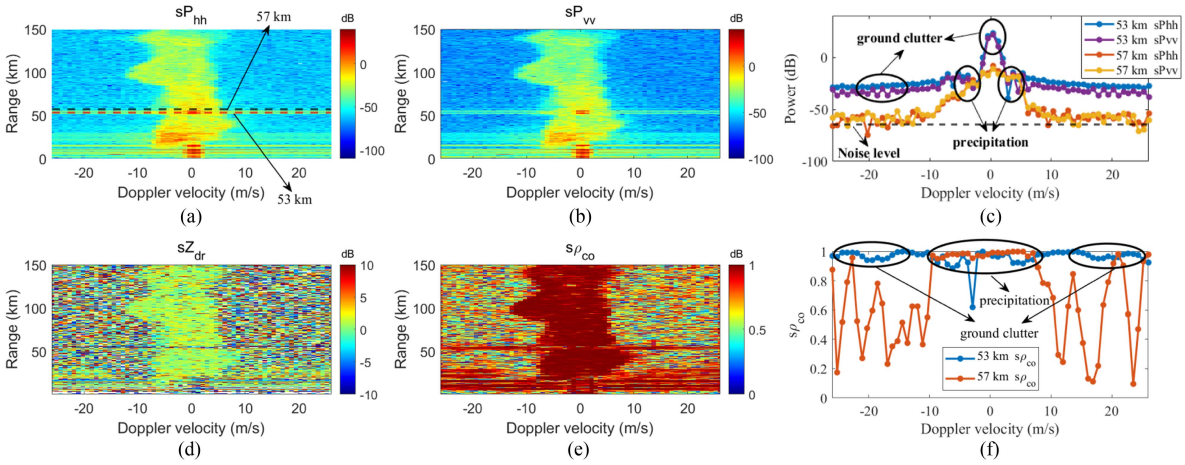

Fig. 3. Observables related to Ray 1 in Fig. 1. (a) Spectral power sP_{hh}. (b) Spectral power sP_{vv}. (c) Power spectrum of range bin 176 (53 km where GC and precipitation overlap) and 189 (57 km where only precipitation exists). (d) Spectral differential reflectivity sZ_{dr}. (e) Spectral copolar correlation coefficient $s\rho_{\mathrm{co}}$. (f) $s\rho_{\mathrm{co}}$ spectrum of range bin 176 and 189.

to the GC power being comparable to or stronger than precipitation [e.g., 53 km in Fig. 3(a) and 3(c)].

5) GC and precipitation have similar correlations [e.g., 53 km in Fig. 3(e) and 3(f)].

These features make it challenging to eliminate clutter for weather radar.

As the red line at 53 km and the black line at 57 km in Fig. 3(a) and 3(c) show, the power of GC is higher than that of precipitation. In addition, the GC increases the noise level in the Doppler domain, and the power of sidelobe clutter is equivalent to precipitation, as indicated by the black line at 53 km and the red line at 57 km in Fig. 3(c). For sZ_{dr}, due to the wide sZ_{dr} distribution of GC, the sZ_{dr} value of GC is diverse, but the sZ_{dr} distribution of precipitation is relatively concentrated around zero [24], as shown in Fig. 3(d). In this case, the $s\rho_{\mathrm{co}}$ values of precipitation and clutter are similar, as Fig. 3(f) shows (53 km where GC and precipitation overlap). This indicates that the GC characteristics make it even harder to suppress, and another parameter should be combined when $s\rho_{\mathrm{co}}$ is used to suppress GC.

III. Proposed Algorithm

Taking advantage of the spectral-polarimetric feature and the RD continuity of precipitation, the proposed approach is implemented in the RD spectrogram. The proposed GC and noise mitigation method can be divided into two stages containing six steps, as shown in Fig. 4. The input of the proposed method is the raw RD spectrogram while the output is the processed one. The raw RD spectrogram is obtained by applying the Fourier transform along the sample time using a Hamming window, considering the Hamming window has less signal-to-noise ratio

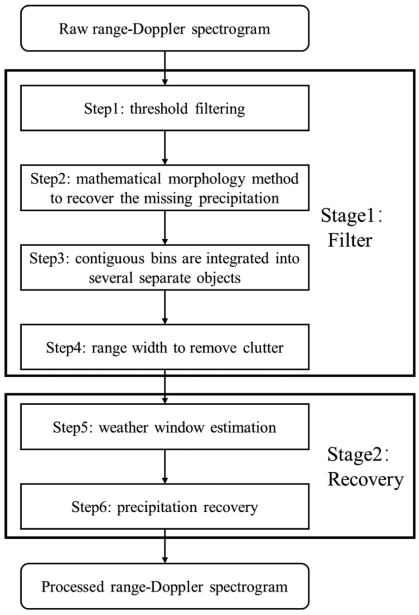

Fig. 4. Flowchart of the proposed method.

(SNR) loss and moderate clutter suppression [9]. The two stages are described in detail ahead.

A. Stage 1: Filtering

The specific steps of stage 1 are as follows.

Step 1: A precipitation mask is obtained by spectral polarimetric filtering.

This step preliminarily removes GC and noise by threshold filtering based on the characteristic difference between precipitation and GC and noise. For operational DP weather radar systems without cross-polar measurements, the spectral copolar correlation coefficient $s\rho_{\text{co}}$ is always known. After being filtered by $s\rho_{\text{co}}$, the binary mask $M^{s\rho_{\text{co}}} \in \{0, 1\}$ indicating precipitation can be expressed as follows:

$$M^{s\rho_{\text{co}}} = \begin{cases} 1, & \text{if } s\rho_{\text{co}} > T_1 \\ 0, & \text{otherwise} \end{cases} \tag{8}$$

where the threshold T_1 can be set based on the clutter and precipitation removal percentage [24], [25].

Since the density function in precipitation and clear air echoes have many overlaps, the $s\rho_{\text{co}}$ threshold processing will retain much GC. When the GC is strong, after applying the Hamming window, the energy of GC mainly concentrates in several Doppler bins near zero Doppler velocity. Therefore, this article uses CPA to identify the GC location, and CPA is calculated by (4). After the GC identification, the narrow notch filter around zero can be applied to the range bins identified as GC to remove the main lobe, and the width of the CPA mask is six central Doppler bins. With such implementation, a mitigation mask $M^{\text{CPA}} \in \{0, 1\}$ indicating GC is expressed as follows:

$$M^{\text{CPA}} = \begin{cases} 0, & \text{if CPA} > T_2 \\ 1, & \text{otherwise} \end{cases} \tag{9}$$

where "0" indicates that there is GC.

It should be noted that $s\rho_{\text{co}}$ filter is applied to the entire spectrogram while the CPA with a narrow notch filter is only concentrated around zero, and the remaining bins will be set to "1" in M^{CPA}.

After Step 1, one binary mask $M_1 \in \{0, 1\}$ can be obtained, which is expressed as follows:

$$M_1 = M^{s\rho_{\text{co}}} \cdot M^{\text{CPA}}. \tag{10}$$

Step 2: The mathematical morphology method is employed to recover the missing precipitation.

The threshold is determined based on the precipitation and clutter removal percentage, so after the threshold filtering, the precipitation can be excessively suppressed, leading to a few holes in the RD spectrogram. This makes the precipitation discontinuous. To address this problem, the missing precipitation is recovered using mathematical morphology, which has been widely used in binary image analyses. In particular, holes inside M_1 are filled in using the dilation operator with the appropriate structuring element. This step extends the perimeter of the RD areas with values "1," which can be restored by performing the erosion operator with the structuring element, and the structuring element is selected as a flat disk of radius 3 [8]; for more details, refer to the work in [8]. After Step 2, a binary mask $M_2 \in \{0, 1\}$ is obtained.

Step 3: The contiguous bins with the value "1" are integrated into several separate objects.

As well known, precipitation always occupies a large area, so the purpose of this step is to preserve the large area as "precipitation," removing scattered points and residual clutter. In general, this step groups contiguous bins with the same value "1" in the RD spectrogram as objects. After this step, only large-size areas and limited numbers of objects will be regarded as "precipitation" [8]. These objects will be selected for further processing in Step 4. After completing the three steps, M_3 can be obtained, which is a matrix consisting of M rows and N columns, where M represents the number of samples in the range, and N is the number of samples in a dwell time. The schematic is shown in Fig. 5(a).

Step 4: The range width is used to remove the residual clutter.

Due to the sidelobe of GC ranging from $-v_{\text{max}}$ to $+v_{\text{max}}$, there might be some GC still left after the first three steps. The objects labeled as precipitation are analyzed to remove the residual sidelobe of GC. The morphological feature of precipitation is distributed along the range in the RD domain while that of GC is distributed along Doppler, as shown in Fig. 2(a) and 2(b). Taking advantage of the difference in distribution between precipitation and GC in the RD spectrogram, this study adds an observable to remove the sidelobe of strong GC. After summing M_3 along the range, the number of points remaining in the range dimension is calculated, and the range width is defined as follows:

$$W^{\text{range}}(n) = \sum_{m=1}^{M} M_3(m, n) \tag{11}$$

where m ranges from one to M, and n ranges from one to N.

From Fig. 5(b), the W^{range} value is large at the velocity where precipitation is located while the W^{range} value of the residual

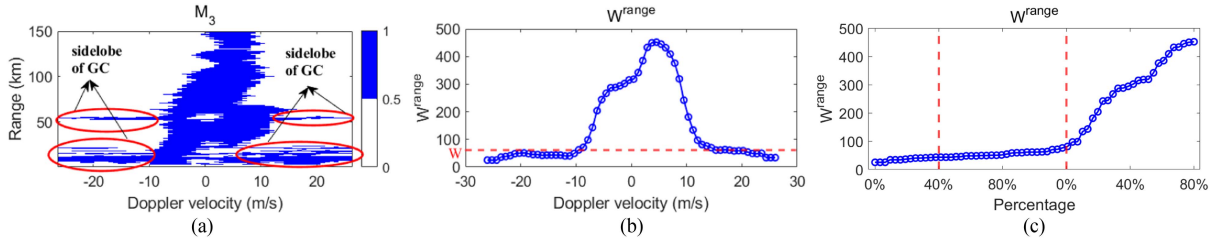

Fig. 5. Schematic drawing. (a) M_3. (b) W^{range}. (c) W^{range} in ascending order.

noise and clutter is minimal. Considering that the sidelobe of GC spreads out to the entire Doppler spectrum, as analyzed in Section II, this study reorganizes the range width in ascending order. As shown in Fig. 5(c), the sorting places the weak component representing the residual clutter and noise on the left while the strong component representing precipitation is placed on the right. Therefore, there are generally two regions: 1) a sidelobe clutter and noise region on the left (i.e., weaker component) and 2) a precipitation region on the right (i.e., larger component). The sidelobe clutter level between the two regions is determined by averaging the range width WW in the range of a% to b%. This idea has been inspired by Siggia and Passarelli [27]. The percentages a% and b% can be set based on the clutter and noise and precipitation distributions after the first three steps. Then, the GC region in binary mask M_3 is replaced by "0." After this step, binary mask M_4 is obtained.

The analysis of the clutter characteristics in Section II shows that GC and precipitation have similar correlations. When precipitation and GC overlap, the aforementioned steps have a tendency to remove the clutter-contaminated precipitation, resulting in biased estimates. To obtain more accurate precipitation observation, this study proposes a reconstruction method to recover precipitation.

B. Stage 2: Precipitation Recovery

Under the assumption that the spatial continuity of precipitation usually occupies a large volume of space compared to the resolution volume of typical weather radars, the spectral characteristics of precipitation from consecutive range bins should be similar [32]. This is particularly true when the radar resolution volume is relatively small. Following this assumption, this study introduces a recovery approach to equalize precipitation using velocity and spectral width continuity. In this stage, precipitation-window estimation and precipitation reconstruction are performed.

Step 5: Precipitation-window estimation.

This step compensates for the velocity and spectral width of precipitation in the missing range bins, considering the range distribution characteristics of precipitation. The precipitation window is used to determine the precipitation area in each range bin.

The final filtering mask M_4 is applied to the raw RD spectrogram to remove clutter and noise. Then, Doppler velocity and spectral width are obtained by (6) and (7), respectively. According to the analysis in Section II, the sidelobe of GC and precipitation have similar correlations. Therefore, the filter stage

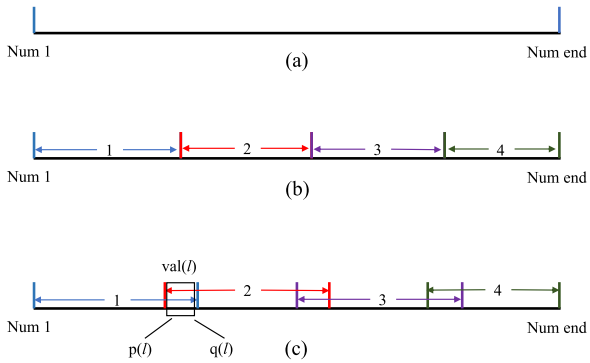

Fig. 6. Sequence segmentation methods. (a) Whole sequence. (b) Four contiguous blocks sequences. (c) Four blocks with some points overlapping.

might result in discontinuity of precipitation. In view of that, this study constructs the Doppler velocity and spectral width based on polynomial interpolation fitting under the assumptions that the precipitation is spatially continuous and that the velocity and spectral width vary slowly at neighboring range bins.

Three types of sequence partition methods are examined using the entire sequence, as illustrated in Fig. 6, where the whole sequence [see Fig. 6(a)], four contiguous sequence blocks [see Fig. 6(b)], and five overlapping sequence blocks (overlapping technique) [see Fig. 6(c)] are presented. This idea has been inspired by Hubbert et al. [30]. As the length of sequences to be fitted increases, high-order polynomial fits are necessary for the variation trend of velocity and spectral width. However, this can be numerically challenging for very high filter orders [30]. Thus, the high-order polynomial fit might not be applicable to long-sequence fitting, and the whole sequence is not selected. Because the initial and final points of the polynomial fitting might have large errors compared with the original data, the method presented in Fig. 6(b) is also not selected. To improve fitting and interpolation accuracy, this study divides the sequence into a series of subsequences with an equal length, fits and interpolates them, and finally combines them into one sequence.

Furthermore, to smooth the overlapped regions, the fitted overlapping points are averaged. Assume that $p(l)$ and $q(l)$ are the first and second overlapping sequences, respectively. Then, the overlapped points need to be combined to form the final sequence, and weights can be expressed as follows:

$$\text{val}(l) = \frac{L+1-l}{L+1}p(l) + \frac{l}{L+1}q(l) \tag{12}$$

where L represents the number of overlapping points.

Considering fitting accuracy and the computational efficiency, the value of L is usually 1/10 of the subsequence length. After determining the coefficients of the polynomial fits for Doppler velocity and spectrum width, the fits are used to estimate the velocity and spectrum width of the contaminated bins. Under the assumption that the frequency spectrum of precipitation has a Gaussian distribution, the precipitation window in the rth range bin can be defined as an interval [32], which can be expressed as follows:

$$[\tilde{v}(r) - K \cdot \tilde{\sigma}_v(r), \tilde{v}(r) + K \cdot \tilde{\sigma}_v(r)] \tag{13}$$

where $\tilde{v}(r)$ and $\tilde{\sigma}_v(r)$ are the fitted mean Doppler velocity and spectrum width in the rth range bin, respectively; K is the precipitation-window width factor. Each spectral coefficient exhibits a large bias in low signal-clutter ratio (SCR) instances, and a small K is essential to mitigate the GC sidelobe. However, for large SCR cases, the bias on each spectral coefficient is small, and a large K is preferred [32]. The K value is evaluated based on the magnitude of the SCR and calculated using the RD regression algorithm. The estimation of the precipitation window takes inspiration from the work in [32], where more details could be found; this method was proposed to mitigate wind turbine clutter by requiring an approximate location of contaminated range bins.

Step 6: Precipitation reconstruction.

The power of precipitation can be overestimated, and the mean radial velocity can be shifted toward zero when there is GC. This has motivated the development of a unified method for mitigating GC and noise and retaining precipitation. This step performs precipitation reconstruction using the Gaussian assumptions of the precipitation power spectrum [27] to ensure the integrity of the precipitation area.

The power spectrum of precipitation can be expressed as follows [27]:

$$S(r,v) = \frac{P(r)}{\sqrt{2\pi}\sigma_v(r)} \exp\left(-\frac{(v(r)-\bar{v}(r))^2}{2\sigma_v^2(r)}\right) + n(r,v) \tag{14}$$

where $P(r)$, $\bar{v}(r)$, and $\sigma_v(r)$ are the spectral-moment estimates of the precipitation in the range r, and $n(r,v)$ denotes the noise power.

Compared with precipitation, GC tends to be stationary, its spectral width is narrow, and its mean Doppler velocity is essentially zero. In contrast, the mean Doppler velocity of precipitation can be any value. The clutter contamination has been conventionally reduced by a notch filter centered at zero. However, this method also suppresses the precipitation, which can lead to bias in spectral moment estimation for precipitation. Therefore, locating GC first and then recovering precipitation using Gaussian fitting to obtain high-quality precipitation is best. The specific flowchart is shown in Fig. 7.

It should be noted that $P(r)$, $\bar{v}(r)$, $\sigma_v(r)$, and $n(r,v)$ are the key elements of Gaussian fitting. The values of $\bar{v}(r)$ and $\sigma_v(r)$ are estimated, as explained in the previous section, and $n(r,v)$ is defined by radar. Thus, the only parameter that needs to be estimated is the peak power $P(r)$, and in this study, it is determined by minimizing the root-mean-square error (RMSE).

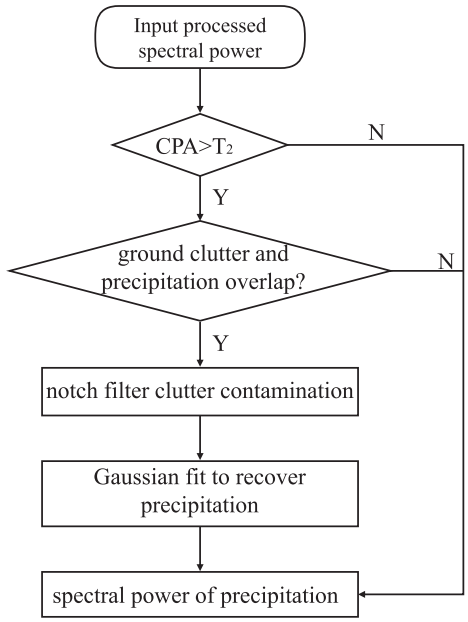

Fig. 7. Flowchart of the precipitation recovery method.

Supposing a spectrogram with I Doppler bins of precipitation after the notch filter, the true power in the vth Doppler bin is $S^{\text{raw}}(v)$. Traversing $P(r)$ between $[P_{r\min}, P_{r\max}]$, where $P_{r\min}$ represents noise power and $P_{r\max}$ is the peak power in the rth range bin, the optimal peak power $P(r)$ of Gaussian fit is obtained by minimizing the RMSE of $S^{\text{raw}}(v)$ and the fitted Gaussian spectrum $S^{\text{est}}(P(r), v)$. The RMSE of the spectral power can be expressed by

$$\delta S(P(r)) = \sqrt{\frac{1}{I}\sum_{v_1}^{v_I}(S^{\text{raw}}(v) - S^{\text{est}}(P(r), v))}. \tag{15}$$

Furthermore, to recover the clutter-contaminated precipitation effectively, the peak power that minimizes the RMSE is set as the peak power of the Gaussian fit.

The proposed approach is used to fill in the gap. Compared with the GMAP [27], the proposed approach can fully use the spatial continuity of precipitation, reducing the amount of calculation. The effectiveness of the proposed method is tested and discussed in the next section.

IV. Performance Evaluation

Datasets were collected by operational weather radar to obtain nearly pure precipitation and clear air. The collected data were used to synthesize several datasets of precipitation combined with clutter with known SCR [14], [15], [16], [17], [18], [19]. The synthesized data were obtained by adding the I&Q data of pure precipitation and clear air; these data were used to compare the clutter suppression performance of the proposed method and several existing algorithms. It should be noted that the pure precipitation data denoted the data after noise removal. The effectiveness of the proposed algorithm was analyzed qualitatively and quantitatively.

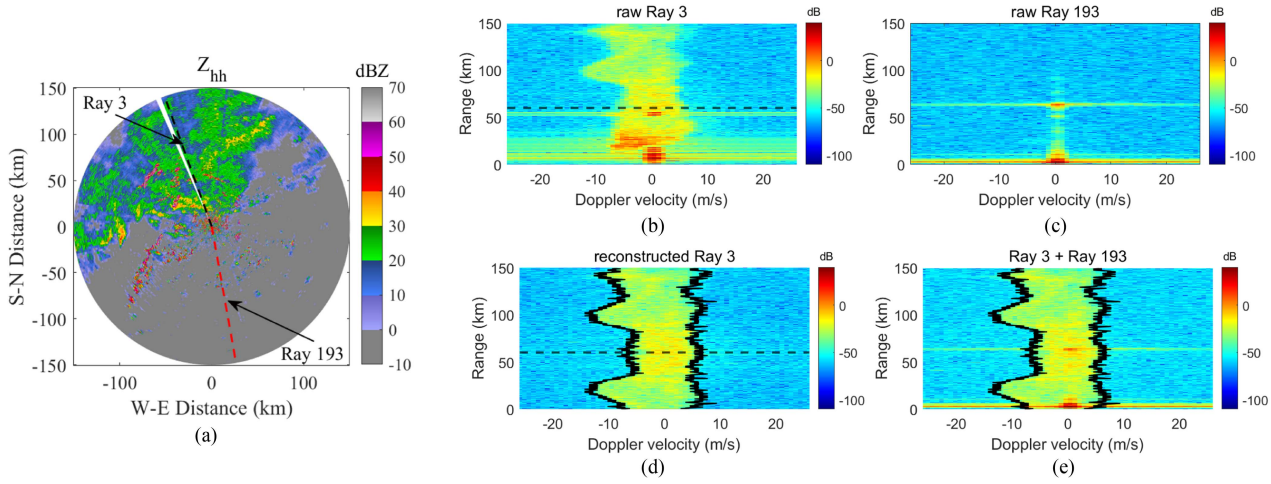

Fig. 8. Construction method description of the combined data acquired using the Ji'an radar. Data were collected at 21:11 on March 5, 2021. (a) Reflectivity PPI. (b) Spectral power sP_{hh} of raw Ray 3. (c) Spectral power sP_{hh} of raw Ray 193 in clear air. (d) Spectral power sP_{hh} of reconstructed pure precipitation for Ray 3. (e) Spectral power sP_{hh} combined pure precipitation with Ray 193.

TABLE II
PARAMETERS OF THE CONSTRUCTED DATASETS

Scenario	Rain	Clear air
Ray number	3,10,16,25,30, 40,47,311,312,317	122,123,124,125,148, 149,157,174,175,193, 194,195,198,244,245, 246,247,248,249,250

TABLE III
RMSE VALUES OF RADAR OBSERVABLES CAUSED BY GC

Case	$\delta\bar{v}$ (m/s)	$\delta\sigma_v$ (m/s)	δZ_{hh} (dB)	δZ_{dr} (dB)
1	2.2	0.7	11.0	2.0
2	2.2	0.7	10.9	2.0
3	1.3	0.9	11.3	2.1
4	2.2	0.7	11.0	2.0
5	0.9	0.7	11.5	2.0
5	0.9	0.7	11.5	2.0
7	4.8	1.6	12.2	2.2
8	3.0	1.8	9.3	2.0
9	3.7	1.1	11.3	2.1
10	3.5	1.0	12.0	2.1
average	2.5	1.0	11.2	2.0
average(200)	2.4	1.0	11.2	2.1

A. Controlled Dataset Construction

The performance of the proposed method was assessed quantitatively using data obtained by Ji'an operational polarimetric weather radar. The raw PPI, shown in Fig. 8(a), included several precipitation rays and clear air rays that helped to find pure precipitation and clear air to construct several datasets with known SCR.

The pure weather data were obtained under precipitation conditions within farther ranges (over 60 km for selected precipitation rays) from the radar location. The GC could be neglected, as Fig. 8(b) shows. The raw spectral power sP_{hh} of clear air is shown in Fig. 8(c). To combine the pure precipitation with clear air, this study folded the data within 60 km as the axis of symmetry to fill in the near precipitation areas, as shown in Fig. 8(d). The combined spectral power sP_{hh} of reconstructed Ray 3 and Raw Ray 193 is shown in Fig. 8(e), and the noise level is calculated using the synthesized datasets [27].

To illustrate the validity and robustness of the proposed algorithm, this study selected 20 sets of clear air data and 10 sets of precipitation data, as shown in Table II. For rainy cases, the true precipitation areas were manually selected in the RD spectrogram [e.g., the black contour in Fig. 8(d) and 8(e)] [8], [25], [26]. Clear air refers to all signals from nonhydrometeors and noise.

These datasets were combined to generate 200 combination datasets. The RMSE was computed for the selected radar observables to measure the GC effect on precipitation and evaluate the clutter and noise suppression and precipitation retention performance of the proposed method. For a given spectrogram, where R range bins were recognized as precipitation, the RMSE of a specific radar observable was calculated by [8], [25], [26]

$$\delta X = \sqrt{\frac{1}{R}\sum_{r=1}^{R}\left(X^{\text{tru}}(r) - X^{\text{est}}(r)\right)^2} \tag{16}$$

where $X^{\text{tru}}(r)$ is the true value of the observable in the rth range bin, which was manually selected, and it is denoted by the black contour in Fig. 8(d); $X^{\text{est}}(r)$ is the corresponding value obtained after combining clear air with precipitation, which is not just in the black contour. It should be noted that the observable X could be $\bar{v}$, σ_v, Z_{hh}, and Z_{dr}.

Ten sets of combined data are randomly selected, and the RMSE of radar observables caused by GC was calculated, as shown in Table III. In addition, we present the average results of the 200 sets of data in the last line.

As shown in Table III, GC caused 2.5 m/s bias in $\bar{v}$, 1.0 m/s bias in σ_v, 11.2 dB bias in Z_{hh}, and 2.0 dB bias in Z_{dr}. It should be noted that the average values within the entire precipitation area were used to calculate the RMSE value. The results showed that the RMSE of the parameters was smaller than the error on the range bins where the real GC was located.

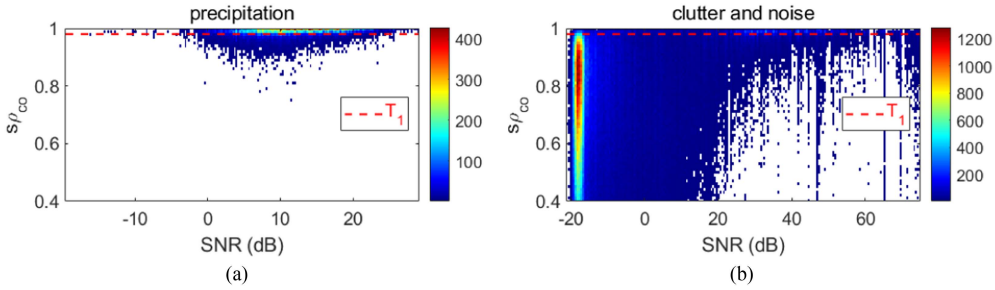

Fig. 9. Scattergrams of $s\rho_{co}$ versus the SNR value for precipitation and nonprecipitation regions. (a) Precipitation. (b) Clutter and noise; the color bars stand for sample numbers; the red dashed line indicates the potential threshold of $s\rho_{co} = 0.98$.

B. Parameter Selection

Retaining precipitation and removing clutter is always a trade-off. Therefore, in Step 1 of the proposed method, $s\rho_{co}$ is used as a spectral polarimetric observable for nonmeteorological scatterer mitigation.

Considering 30 rays of raw PPI in Fig. 8(a), the dataset was classified into two scenarios, namely 1) rain and 2) clear air, as shown in Table II. The $s\rho_{co}$ distribution versus the SNR value was calculated, as shown in Fig. 9. However, since the proposed method was implemented in the spectral domain, the SNR was defined as follows [8]:

$$\mathrm{SNR}(r) = \frac{\sum_{v\in \mathrm{pre}} \left(sP_{\mathrm{hh}}(r,v) - sN\right)}{\sum_{v} sN}. \tag{17}$$

Therefore, one SNR was calculated for each range bin, corresponding to several spectral polarimetric observable values. The noise estimation was based on the noise measurement data obtained by the radar system. In Fig. 9(a) and 9(b), it can be observed that the $s\rho_{co}$ value of precipitation was mostly greater than 0.98. However, the $s\rho_{co}$ value of clutter and noise had a large distribution with the decrease in the SNR value, and most $s\rho_{co}$ values were under 0.98. Specifically, threshold T_1 was set to 0.98 for Ji'an radar based on the precipitation and clutter removal percentage [8], [24], [25], and in this case, it can retain 80% of the precipitation and filter out 93% of the GC. Furthermore, in Fig. 9(b), it can be seen that some $s\rho_{co}$ values of clutter and noise were distributed between 0.98 and one, which indicated that the other observations should be used for clutter and noise suppression.

Considering similar $s\rho_{co}$ distributions of clutter and precipitation, the CPA was used for GC identification. The CPA value of GC was close to one due to its zero velocity and narrow spectral width. The CPA distribution versus mean velocity was calculated in clear air, as shown in Fig. 10, where it can be seen that the CPA value decreased with the velocity, which indicated low CPA for precipitation. A considerable number of points had CPA values exceeding 0.88, so a CPA threshold of 0.88 was used to identify the stable clutter, and in this case, the targeted false alarm rate for the precipitation is less than 1% due to the precipitation having a lower CPA value (mostly less than 0.5) [12], [13]. The threshold selection method is described in detail in [12] and [13]. However, a false alarm could occur on the narrow-band zero-velocity weather signal [13].

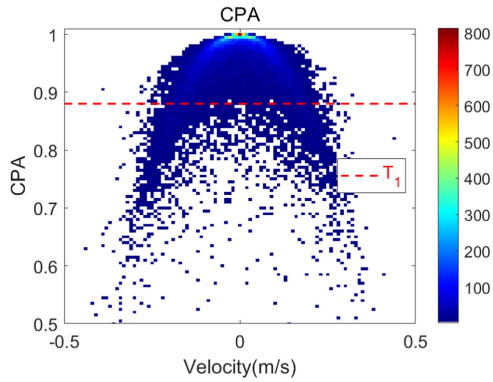

Fig. 10. CPA scattergrams versus velocity for nonprecipitation regions. The red dashed line indicates the potential threshold of CPA = 0.88.

Furthermore, considering the characteristics of GC, W^{range} and WW are used to remove the sidelobe of strong GC and noise. The value of W^{range} in the 200 controlled datasets is shown in Fig. 11. In Fig. 11(a) and 11(c), it can be seen that after the first three steps, the sidelobe of the strong GC still remained. Then, the W^{range} is reorganized in ascending order. Its mean values are shown in Fig. 11(b) and 11(d), where there are generally two regions: 1) a sidelobe clutter and noise region on the left and 2) a precipitation region on the right. And it can be seen that W^{range} of most precipitation is concentrated from 70% to 100% while that of extra GC was below 60%. Particularly, the percentage to determine WW is set to 20%–70% based on the sidelobe of strong GC removal percentage. In a more general sense, the threshold selection method involves determining the intervals for clutter sidelobe width and precipitation target width. Subsequently, the width of the sidelobe clutter is determined using the mean width of nonprecipitation areas. This method is similar to the approach described in [27] for dynamically determining noise levels.

For the threshold selection of $s\rho_{co}$ and CPA, which are the parameters for precipitation/clutter identification, we determine the threshold based on the ratio of retained precipitation to clutter and noise removal [7], [8], [12], [13], [24], [25], [26]. The selection of sidelobe clutter and noise may vary depending on different datasets, meaning the morphology depicted in Fig. 11(c) might slightly change with varying data. However, the general trend after sorting remains consistent with Fig. 11(d). Therefore, we employ a dynamic clutter width selection method

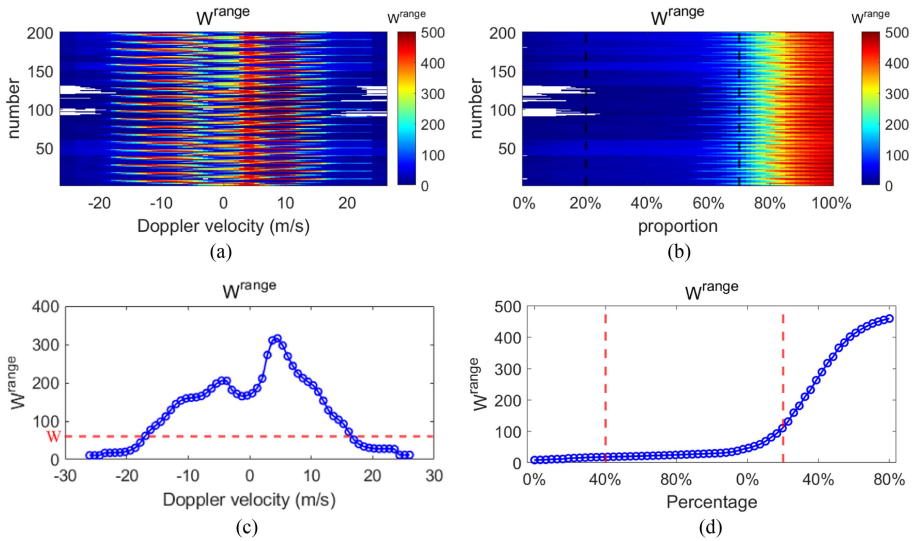

Fig. 11. Value of W^{range} in the 200 combined datasets. (a) W^{range}. (b) W^{range} in ascending order. (c) Mean value of W^{range} in the 200 combined datasets. (d) Mean value of W^{range} in ascending order.

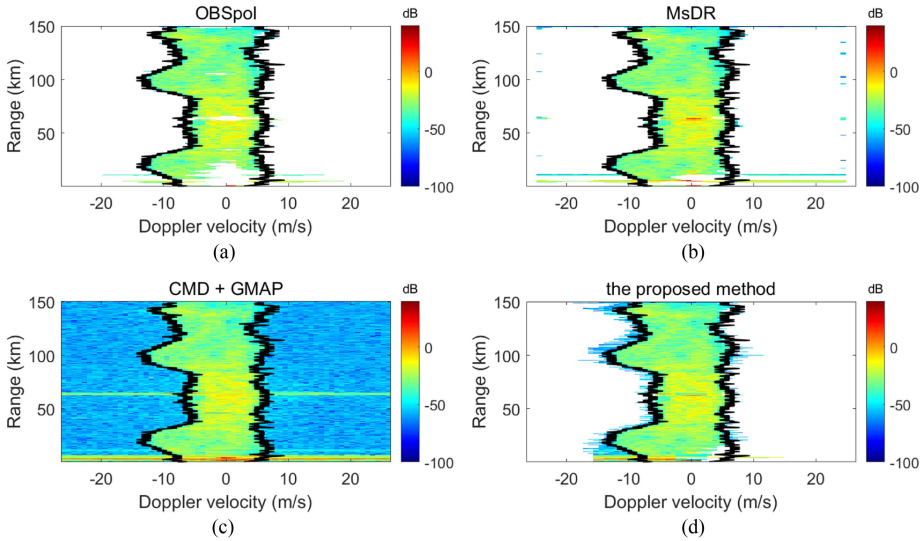

Fig. 12. RD spectrograms after applying different techniques to the combined spectrogram in Fig. 8(e). (a) OBSpol filter. (b) MsDR filter. (c) Method that combined CMD with GMAP. (d) Proposed method.

where the widths obtained after the first three steps are arranged in ascending order. Based on this result, we differentiate between precipitation and nonprecipitation areas and utilize the average width of nonprecipitation regions to determine the threshold for clutter and noise width. The selected variable thresholds can be applied only to this dataset, but this section introduces a general method to select parameter thresholds. This method allows the thresholds to be selected adaptively according to a specific geographical environment surrounding the radar.

C. Clutter Detection Performance Evaluation

To illustrate the effectiveness of the proposed method, this study compared the proposed algorithm with three algorithms, namely the OBSpol, MsDR, and CMD combined with GMAP, both qualitatively and quantitatively. The results of the four algorithms implemented on the combined spectrogram presented in Fig. 8(e) are shown in Fig. 12. Note that the OBSpol method is implemented based on the details provided in [8], where the initial step involves using $s\rho_{\text{co}}$ to detect precipitation and a notch filter to remove GC. The CMD method is replicated following the relevant information in [12] and [13], utilizing CPA, TDBZ (the texture of the reflectivity), and SPIN (the spatial variability of the reflectivity field). Additionally, the GMAP method is replicated according to the relevant content in [27], incorporating adaptive window selection. The results of the four algorithms implemented on the combined spectrogram presented in Fig. 8(e) are shown in Fig. 12.

In Fig. 12(a) and 12(b), it can be seen that both the OBSpol filter and MsDR filter could retain the precipitation from GC while filtering out the noise and clutter. When the GC sidelobe ran through the precipitation, the OBSpol filter tended to filter out

TABLE IV
AVERAGE ERROR OF THE OBSERVABLES PROCESSED BY THE FOUR METHODS

Parameter	Method									
	No		OBSpol		MsDR		CMD + GMAP		Proposed	
	10	200	10	200	10	200	10	200	10	200
P_d	——	——	79.9%	82.1%	89.2%	90.2%	——	——	**90.5%**	**91.5%**
P_{fa}	——	——	**5.2%**	**4.4%**	11.1%	9.3%	——	——	5.6%	5.1%
$\delta\bar{v}$ (m/s)	2.5	2.4	1.9	1.8	2.3	2.1	1.8	1.8	**1.0**	**0.9**
$\delta\sigma_v$ (m/s)	1.0	1.0	1.5	1.4	1.2	1.2	1.8	1.7	**0.5**	**0.7**
δZ_{hh} (dB)	11.2	11.2	**3.8**	4.6	8.0	8.5	4.8	5.3	3.9	**4.2**
δZ_{dr} (dB)	2.0	2.1	**1.2**	**1.3**	2.3	2.1	2.2	2.1	1.8	1.7

The bold values means that the processing result is the best.

the overlapped areas, whereas the MsDR filter might retain some clutter. This was because both the OBSpol filter and MsDR filter could not handle the situation where the precipitation overlapped with GC. As shown in Fig. 12(c), the method that combined CMD with GMAP could reduce the GC power, but the sidelobe and noise were retained. This is mainly due to the prerequisite assumption that the shape of the clutter is approximately Gaussian for the implementation of the GMAP algorithm [27]. However, in the 62.4–64.5 km range, the GC on some range bins exhibits significant fluctuations. This means that the GC on these range bins exhibits multiple spectral components, so the power spectrum exhibits multiple peaks rather than a Gaussian shape. Consequently, the clutter with nonzero velocity and noise still persists within these regions. Furthermore, as shown in Fig. 12(d), although the proposed method retained a portion of GC, it could suppress GC overlapped with precipitation as much as possible.

To evaluate the quality of the polarimetric variable quantitatively, this study used 10 sets of combined data in Table III. In addition, to quantify the performance, the probability of detection (P_d) and false alarm rate (P_{fa}) were calculated as follows [8], [25]:

$$P_d = \frac{\mathrm{TP}}{\mathrm{TP} + \mathrm{FN}} \tag{18}$$

$$P_{fa} = \frac{\mathrm{FP}}{\mathrm{FP} + \mathrm{TN}} \tag{19}$$

where TP is the number of precipitation bins that were accurately identified; FN is the number of precipitation bins that were classified as clutter or noise; FP is the number of clutter and noise bins that were classified as precipitation; TN is the number of clutter and noise bins that were successfully identified.

It should be noted that the true area was obtained by the manual selection of precipitation in the reconstructed RD spectrogram [8], [25]. It is also worth noting that the method that combined CMD with GMAP was not involved in this evaluation, as it was not selecting the precipitation, as shown in Fig. 12(c).

The RMSE value was computed for the selected radar variables, but $X^{\mathrm{est}}(r)$ denoted the corresponding value after applying the methods. P_d, P_{fa}, RMSE of $\bar{v}$, σ_v, Z_{hh}, and Z_{dr} are shown in Table IV. Table IV presents only the average error on the 10 and 200 sets of combined data listed in Table III before and after applying the four methods. Note that the "No" column represents the deviation in precipitation parameter estimation resulting from the combination of pure precipitation and clear air, where "No" indicates no clutter suppression techniques applied.

After using the OBSpol filter, the average $P_d(79.9\%)$, $P_{fa}(5.2\%)$, δZ_{hh}(3.8 dB), and δZ_{dr}(1.2 dB) were the smallest among all techniques. The P_d value of the OBSpol filter was only 79.9%, which indicated that when GC was overlapped with precipitation, the OBSpol filter tended to remove GC that overlapped with precipitation. This could result in precipitation loss and lead to bias in precipitation parameter estimation, as shown in Fig. 12(a). Apart from that, the result of the smallest error was used as an estimation parameter, and it was calculated using the remaining precipitation. The average $\delta\sigma_v$ of the OBSpol filter was 1.9 m/s because of the precipitation loss. By contrast, the average $\delta\bar{v}$ (2.3 m/s), δZ_{hh} (8.0 dB), and δZ_{dr} (2.3 dB) were the largest among all processing techniques, which was due to clutter retention in the MsDR filter, as shown in Fig. 12(b). The average $\delta\bar{v}$, δZ_{hh}, and δZ_{dr} of the CMD and GMAP were 1.8 m/s, 4.8 dB, and 2.2 dB, respectively; there was the RMSE difference because of the GC sidelobe retention in the CMD and GMAP processing. Compared with the other techniques, after the proposed method processing, the average P_d (90.5%) was the largest, and the average $\delta\bar{v}$ (1.0 m/s) and $\delta\sigma_v$ (0.5 m/s) were the smallest. For weather radar, the precipitation retention performance is as important as the clutter suppression performance. Therefore, although the average δZ_{hh} and δZ_{dr} of the proposed method were comparable with those obtained after applying the OBSpol filter and the method that combined CMD with GMAP, the overall performance of the proposed method was the best among all methods. The results indicated that the proposed method could maintain most of the precipitation while removing the majority of clutter and noise.

It is worth noting that after applying the other three algorithms, $\delta\sigma_v$ was larger compared with the raw situation. As well known, strong GC might shift the σ_v value toward zero. For the OBSpol filter and the MsDR filter, there was an increase in the $\delta\sigma_v$ value due to the precipitation loss and the sidelobe of GC retention. However, the method that combined CMD with GMAP could reduce the main lobe of GC, but the sidelobe spread out to the entire Doppler spectrum was retained, which could enlarge σ_v causing $\delta\sigma_v$ be larger than that of untreated.

As shown in Fig. 8(e), the GC power was approximately 60 dB greater than that of precipitation. This implied that any residual

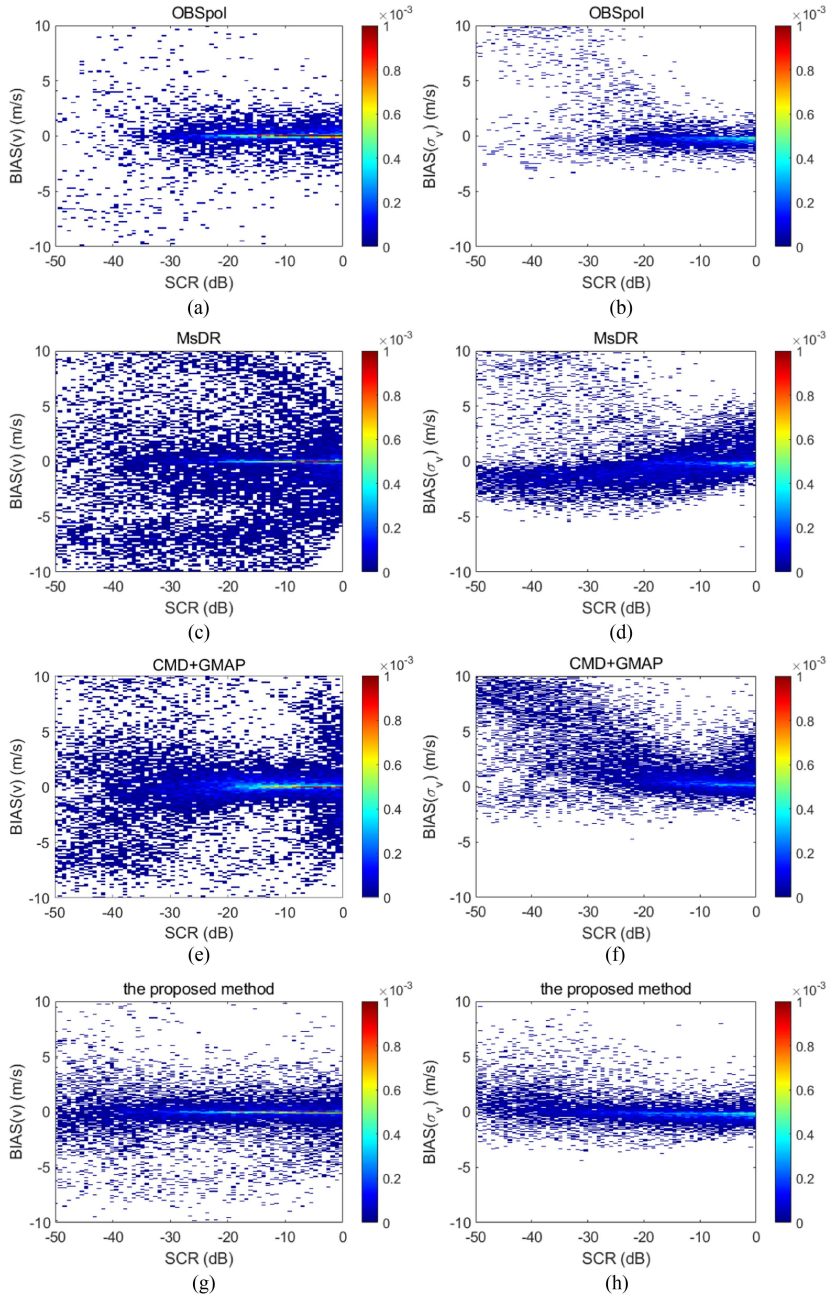

Fig. 13. Distribution of $\bar{v}$ and σ_v bias versus the SCR. (a) and (b) Results after applying the OBSpol filter. (c) and (d) Results after applying the MsDR filter. (e) and (f) Results after applying the method that combined CMD with GMAP. (g) and (h) Results after applying the proposed method. Note that the color bar represents the probabilities.

or excessive estimation of GC could cause a large deviation. Therefore, to analyze the changing trend of the estimation bias of $\bar{v}$ and σ_v with SCR, the estimation error was defined as follows [1], [9], [34]:

$$\mathrm{BIAS}(\hat{X}(r)) = X^{\mathrm{est}}(r) - X^{\mathrm{tru}}(r) \tag{20}$$

where $X^{\mathrm{tru}}(r)$ is the true value of the observable at the rth range bin, and $X^{\mathrm{est}}(r)$ is the estimated value of the observable at the rth range bin.

It should be noted that the observable X could be $\bar{v}$ and σ_v, and when $X^{\mathrm{est}}(r)$ was closer to $X^{\mathrm{tru}}(r)$, the value of $\hat{X}(r)$ was smaller. The $\bar{v}$ and σ_v distribution versus the SCR are shown in Fig. 13. The SNR, CNR, and SCR were, respectively, defined as follows:

$$\mathrm{SNR}(r) = \frac{\sum_v \left(sP_{\mathrm{hh}}^{\mathrm{pre}}(r,v) - sN\right)}{\sum_v sN} \tag{21}$$

$$\mathrm{CNR}(r) = \frac{\sum_v \left(sP_{\mathrm{hh}}^{\mathrm{clu}}(r,v) - sN\right)}{\sum_v sN} \tag{22}$$

$$\mathrm{SCR}(r) = \mathrm{SNR}(r) - \mathrm{CNR}(r) \tag{23}$$

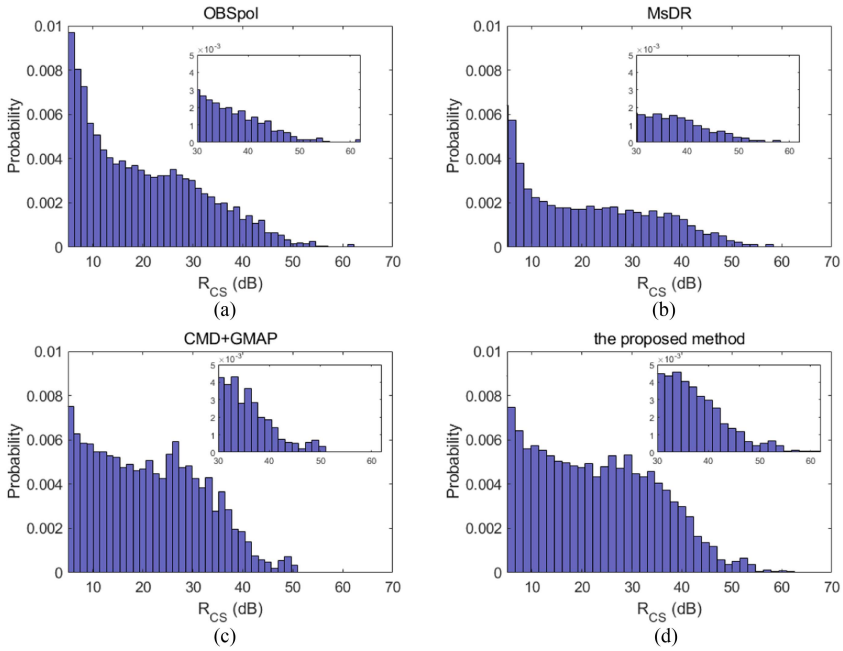

Fig. 14. R_{CS} histograms after applying the four methods:. (a) OBSpol filter. (b) MsDR filter. (c) Method that combined CMD with GMAP. (d) Proposed method.

where $sP_{\mathrm{hh}}^{\mathrm{pre}}$ represents the spectral power of pure precipitation with hh polarization, and $sP_{\mathrm{hh}}^{\mathrm{clu}}$ represents the spectral power of clear air with hh polarization.

In addition, the SNR was calculated using the reconstructed spectral power, which was considered pure precipitation; the CNR was calculated in the clear-air condition; the SCR of the combined data was calculated by (23).

Fig. 13 shows the bias of $\bar{v}$ and σ_v when the SCR was less than or equal to zero. It can be observed that relative to the other three methods, the proposed method exhibits the most concentrated estimation bias toward 0 m/s for $\bar{v}$ and σ_v. Fig. 13(a) and 13(b) indicates that, with the OBSpol method, the bias in $\bar{v}$ and σ_v is also relatively concentrated when SCR> -30 dB. However, there are few signals when SCR < -30 dB, as this method tends to filter out signals in the overlapped areas. The MsDR method yields more signals after processing, but the bias in the processed signals is relatively dispersed, primarily because MsDR tends to retain signals in the overlapped areas. The method that combined CMD with GMAP does not cause signal loss, and the bias in $\bar{v}$ and σ_v is relatively concentrated. However, this algorithm cannot completely eliminate GC and spectral leakage when GC is strong and fluctuating, as shown in Fig. 12(e). Hence, the estimation bias of signals when SCR< -30 dB tends to be more dispersed and relatively larger. As mentioned earlier, the proposed method demonstrates better performance in clutter and noise suppression and precipitation retention.

To further quantify the performance of the proposed method, the clutter suppression ratio (R_{CS}) [25], [26] of the 200 cases combined with pure precipitation and clear air was calculated, as shown in Fig. 14. In principle, R_{CS} was the filtered reflectivity subtracted from the raw one. For the OBSpol filter, the maximum R_{CS} was 63 dB, and the probability of R_{CS} values larger than 30 dB was 2.3%. For the MsDR filter, the maximum R_{CS} was 62.9 dB, which was equal to that of the OBSpol filter, and the probability of R_{CS} values larger than 30 dB was 1.5%. For the algorithm that combined CMD with GMAP, the maximum R_{CS} was 50.9 dB, and the probability of R_{CS} values larger than 30 dB was 3%. However, the maximum R_{CS} of the proposed method is 62 dB, which was equal to those of the OBSpol and MsDR filters, and the probability of R_{CS} values larger than 30 dB was 3.7%, which was the largest among the four algorithms. In addition, after processing with different methods, the average R_{CS} for adding the same power is shown in Fig. 15. As can be seen from Fig. 15, R_{CS} of the proposed method is relatively high. The R_{CS} result indicated that the proposed method was more effective than the other algorithms in clutter suppression.

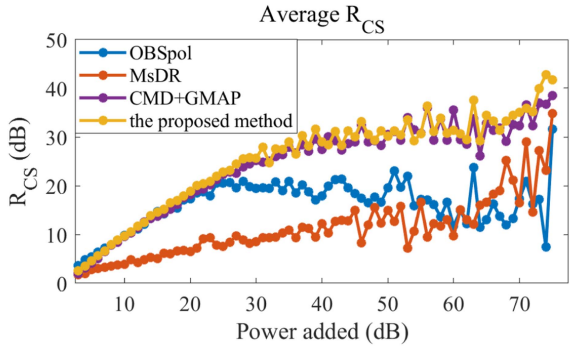

Fig. 15. Relationship between R_{CS} and added clutter power.

This section illustrates the effectiveness of the proposed algorithm quantitatively using the constructed data with known SCR. In parameter estimation, the proposed method obtained the maximum detection probability and the minimum RMSE of $\bar{v}$ and σ_v compared with the other three methods, which

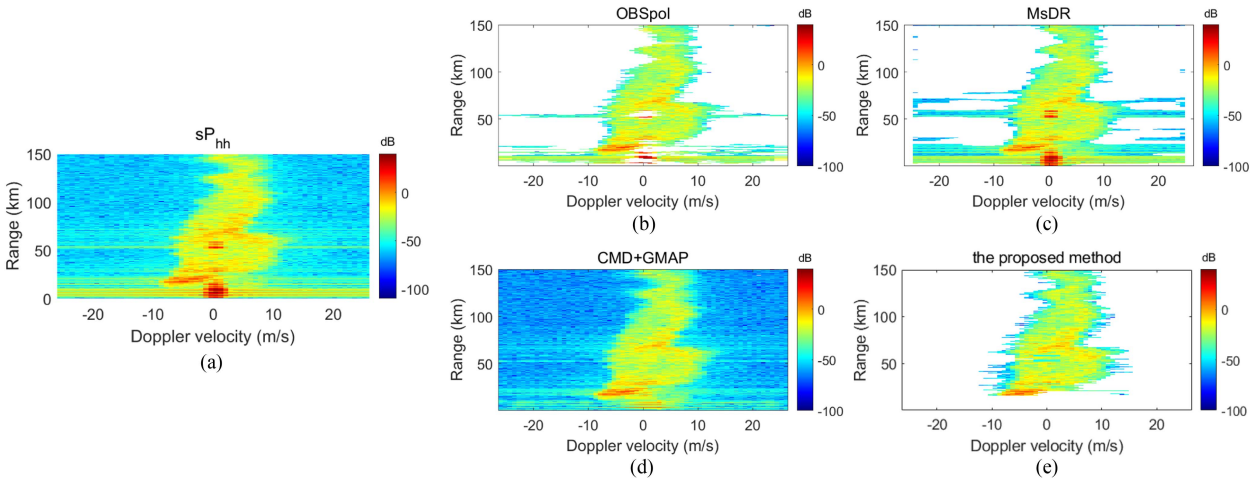

Fig. 16. Qualitative performance comparison of the OBSpol filter, the MsDR filter, the method that combined CMD with GMAP, and the proposed method. The presented RD spectrogram is the spectrogram corresponding to the data of Ray 21 in Fig. 8(a). (a) Raw spectrogram. (b) OBSpol filtered spectrogram. (c) MsDR-filtered spectrogram. (d) Spectrogram after applying the method that combined CMD with GMAP. (e) Spectrogram after the proposed method processing.

represented the best precipitation retention performance. Meanwhile, the RMSE of $Z_{\rm hh}$ and $Z_{\rm dr}$ could also be reduced to a large extent. As for $R_{\rm CS}$, the proposed method had a larger number of points with an $R_{\rm CS}$ value greater than 30 dB, indicating the best clutter suppression performance.

D. Spectrogram Analysis

The results of the four methods implemented on the raw RD spectrogram $sP_{\rm hh}$ of Ray 21 are shown in Fig. 16. As presented in Fig. 16(b) and 16(c), both the OBSpol filter and the MsDR filter could not resolve the problem when precipitation and clutter overlapped. In addition, as shown in Fig. 16(a), when the GC power was very high, and the power of sidelobe was up to -10 dB, which was similar to or higher than precipitation, it was impossible to determine whether there was precipitation. In this situation, the method that combined CMD with GMAP could reduce the clutter power significantly, but some clutter still remained due to strong GC completely masking the precipitation. The proposed method outperformed the other methods, keeping many weak signals while recovering the clutter-contaminated precipitation. However, GC was so strong within 20 km that it was impossible to determine whether it contained precipitation, so the proposed method removed the signal of this area. Overall, the clutter suppression performance of the proposed method was better than that of the other three methods.

E. PPI Analysis

For operational weather radar systems, the filtered observables are required to be displayed in radar PPI. Therefore, to test the proposed technique's performance, this study applied the four methods to the data shown in Fig. 8(a). Compared with the PPI result after the OBSpol filtering, which is shown in Fig. 17(a), $Z_{\rm hh}$ of the proposed method was much higher, indicating better performance in precipitation retention. In addition, compared with the PPI result after the MsDR filtering, which is shown in Fig. 17(c), the proposed method achieved better performance in clutter removal. Furthermore, as shown in Fig. 17(e) and 17(g), the performances of the method that combined CMD with GMAP and the proposed method were comparable. For the area near the radar, where GC was present throughout the spectrum, the method that combined CMD with GMAP might keep some GC, thus leading to bias in $Z_{\rm hh}$ and v. However, when GC was so strong that it was impossible to determine whether it contained precipitation, the proposed method tended to remove the signal, as shown in Fig. 16; thus, there could be partial signal loss in the near areas in Fig. 17(g) and 17(h).

Finally, the performance comparison between the proposed method and the method that combined CMD with GMAP presented in this section is similar to that in [2], where the comparison between the GMAP-TD and the GMAP was conducted.

V. Method Application to Guangzhou Radar

In this section, the performance of the proposed method is further discussed both qualitatively and quantitatively. To illustrate the robustness of the proposed method, this study used the data collected by another operational DP weather radar located in Guangzhou, China. The system specifications of this radar are the same as those of the Ji'an radar used in the aforementioned analyses.

The parameter selection in the proposed method was performed as presented in Section IV, as shown in Fig. 4. For Guangzhou radar, the threshold of $s\rho_{\rm co}$ was set to 0.98, CPA was set to 0.88, and the percentage to determine WW was set to 20%–70%.

A. Spectrogram Analysis

The results of the four methods implemented on the raw RD spectrogram $sP_{\rm hh}$ of Ray 131 are shown in Fig. 18. The results indicated that the OBSpol and MsDR filters could not resolve the

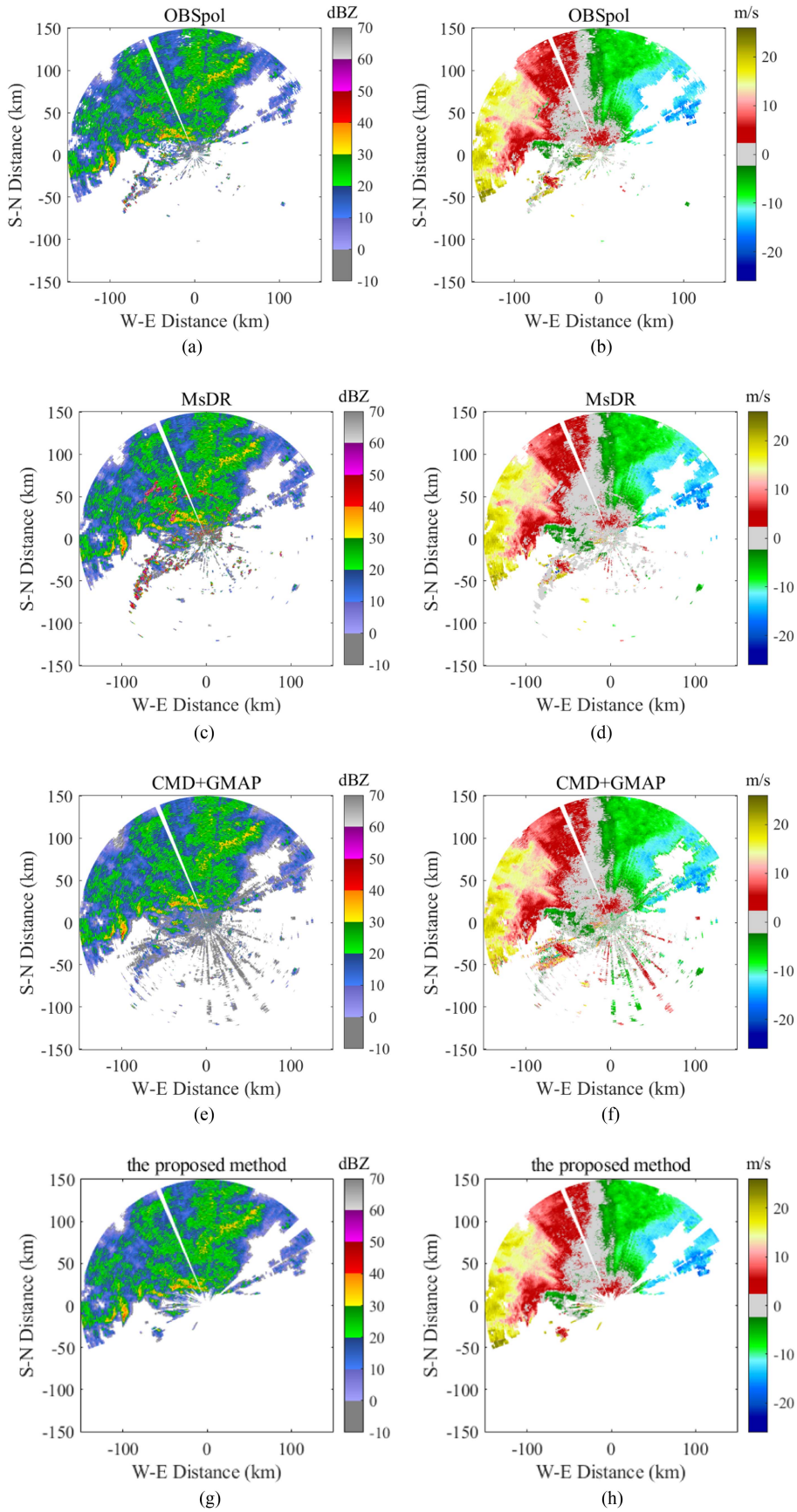

Fig. 17. PPI comparison results of Z_{hh} and $\bar{v}$ processing performance. Data are the same as in Fig. 1 and were collected at 21:11 on March 5, 2021. (a), (c), (e), and (g) Results of Z_{hh}. (b), (d), (f), and (h) Results of $\bar{v}$.

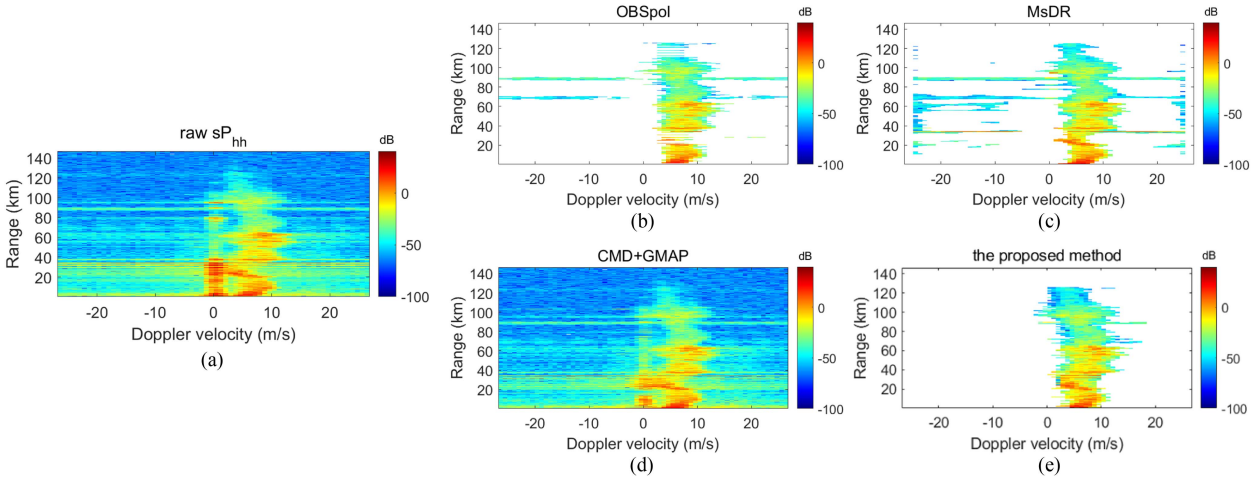

Fig. 18. Qualitative performance comparison results of the OBSpol filter, the MsDR filter, the method that combined CMD with GMAP, and the proposed method. The RD spectrogram represents the spectrogram corresponding to the data of Ray 131; the data were measured by the Guangzhou radar at 5:30 on May 20, 2016. (a) Raw spectrogram. (b) OBSpol-filtered spectrogram. (c) MsDR-filtered spectrogram. (d) Spectrogram after applying the method that combined CMD with GMAP. (e) Spectrogram after the proposed method processing.

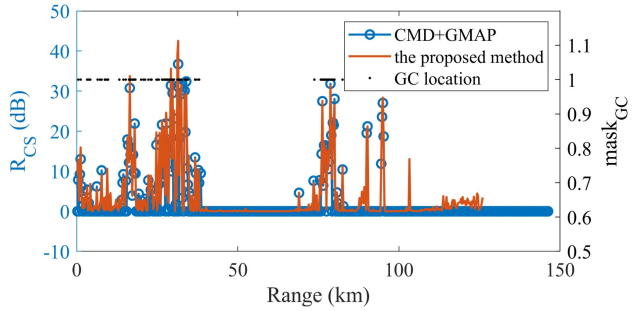

Fig. 19. R_{CS} results of the method that combined CMD with GMAP and the proposed method.

problem when precipitation and clutter overlapped. In addition, the results in Fig. 18(b) and 18(c) indicate that both filters could preserve most of the precipitation, but they also retained too much clutter and noise. Furthermore, as shown in Fig. 18(d), the method that combined CMD with GMAP retained much GC. The R_{CS} values of this method and the proposed method are shown in Fig. 19, where it can be seen that the GC mitigation performance of the proposed method was comparable or even better than that of the method that combined CMD with GMAP. The result demonstrated that the proposed method performed better in terms of clutter suppression and precipitation retention than the other methods.

To quantify the performance further, P_d, P_{fa}, and RMSE of $\bar{v}$, σ_v, and Z_{hh} were calculated. Note that the GC and precipitation are manually selected [7], [8], [25], [26]. The P_d and P_{fa} results are shown in Table V. It should be noted that the method that combined CMD with GMAP was not involved in this evaluation. The RMSE results of $\bar{v}$, σ_v, and Z_{hh} are shown in Table VI.

As presented in Table V, the average P_d and P_{fa} values of the MsDR were 95.5% and 40.9%, respectively; meanwhile, the OBSpol achieved the average P_d and P_{fa} values of 95.4% and 61.1%, respectively. The P_d results of the two filters could be up to 95%, which indicated that these methods could preserve much more precipitation. However, the P_{fa} value was relatively large

TABLE V
P_D AND P_{FA} RESULTS OF RADAR OBSERVABLES

Ray Num	OBSpol		MsDR		Proposed	
	P_d	P_{fa}	P_d	P_{fa}	P_d	P_{fa}
3	97.9%	69.6%	97.7%	54.2%	99.7%	9.3%
27	91.3%	45.7%	95.3%	27.6%	99.9%	3.2%
56	96.9%	68.0%	93.5%	41.0%	99.9%	6.7%
average	95.4%	61.1%	95.5%	40.9%	**99.9%**	**6.4%**

The bold values means that the processing result is the best.

due to the incomplete clutter and noise suppression. The results improved after using the proposed algorithm, achieving the P_d and P_{fa} values of 99.9% and 6.4%, respectively. This indicated that the proposed method retained most of the precipitation and filtered out almost all the clutter and noise. In conclusion, the proposed method performed well in clutter and noise suppression and precipitation retention.

As shown in Table VI, the average δZ_{hh} values of the previous three methods were 1.2, 0.7, and 0.7 dB while that of the proposed method was 0.3 dB. Apart from that, the average $\delta\bar{v}$ and $\delta\sigma_v$ values of the proposed method were both 0.5 m/s, which was the smallest results among the four methods.

B. PPI Analysis

Next, to test the performance of the proposed method further, the four methods were applied to the data collected at 5:30 CST on May 20, 2016; the results are shown in Fig. 20. Compared with the PPI values after the OBSpol and MsDR filtering processes, the proposed method performs better in precipitation retention and clutter removal. As shown in Fig. 20(d) and 20(e), the performances of the method that combined CMD with GMAP and the proposed method were comparable. For the areas near the radar, the method that combined CMD with GMAP could keep some GC leading to errors in Z_{hh}. However, the proposed method could lose some precipitation.

TABLE VI
RMSE RESULTS OF RADAR OBSERVABLES

Ray No	OBSpol			MsDR			CMD + GMAP			Proposed		
	$\delta\bar{v}$	$\delta\sigma_v$	δZ_{hh}	$\delta\bar{v}$	$\delta\sigma_v$	δZ_{hh}	$\delta\bar{v}$	$\delta\sigma_v$	δZ_{hh}	$\delta\bar{v}$	$\delta\sigma_v$	δZ_{hh}
3	2.6	2.4	1.3	2.4	2.4	0.5	2.2	2.7	0.7	0.2	0.5	0.1
27	2.4	0.9	1.4	2.2	1.0	0.9	1.2	1.6	0.6	0.3	0.2	0.1
56	1.5	1.1	1.0	1.6	1.1	0.9	1.5	1.9	0.7	1.0	0.7	0.6
average	2.1	1.5	1.2	2.1	1.5	0.7	1.6	2.1	0.7	0.5	0.5	0.3

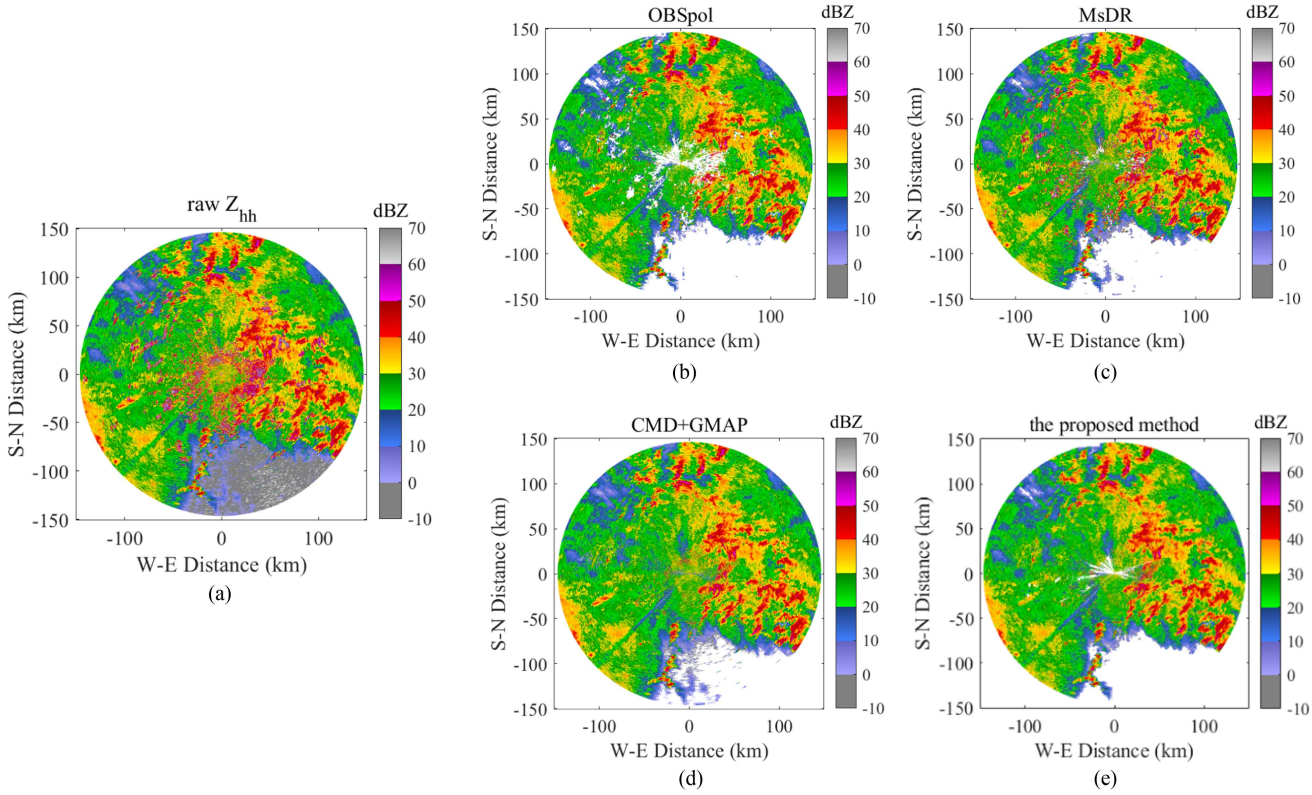

Fig. 20. PPI processing performance comparison of the four methods. Data were collected by Guangzhou radar at 5:30 on May 20, 2016. (a) Raw Z_{hh}. (b) Z_{hh} after applying the OBSpol filter. (c) Z_{hh} after applying the MsDR filter. (d) Z_{hh} after applying the method that combined CMD with GMAP. (e) Z_{hh} after applying the proposed method.

The PPI comparison of other radar products (i.e., Z_{dr}, $\bar{v}$) is shown in Fig. 21. After the proposed method processing, most of the clutter and noise were removed from the radar PPI, and the majority of precipitation was successfully preserved. As shown in Fig. 21(a) and 21(b), there were fewer anomalous points in Z_{dr} after the proposed method was applied. Comparing the results displayed in Fig. 21(c) and 21(d), it can be concluded that the raw velocity had a large number of outliers while the radial velocity became more continuous after the proposed method was applied. Moreover, it can be seen that the spectral polarimetric filter and precipitation recovery using spectral moments improved the accuracy of the observation.

C. Other Case Study

Finally, another case study was conducted to illustrate the performance and robustness of the proposed method. This case study used data collected at 5:31 CST on May 20, 2016, at an elevation of 1.5°. The raw PPI of Z_{hh}, $\bar{v}$, and Z_{DR} is shown in Fig. 22(a)–22(c), respectively, where it can be seen that GC could increase the power, causing the Z_{DR} errors and shifting the velocity toward zero. The PPI of Z_{hh} after the proposed method processing is shown in Fig. 22(d), where it can be observed that the proposed method could effectively suppress GC in the near areas with less precipitation loss. The PPI of Z_{DR} after the proposed method processing is shown in Fig. 22(e), where it can be seen that this method could eliminate the errors caused by GC. Fig. 22(f) displays the processed radial velocity, demonstrating that the velocity was smoother compared with the raw. Moreover, Ray 90 was used as an analysis instance to better illustrate the algorithm's effectiveness. The spectrograms before and after applying the four methods to Ray 90 data are shown in Fig. 23.

As shown in Fig. 23(a), the measurement was influenced by GC. Both the MsDR and OBSpol filters could remove most of the clutter and noise. However, the OBSpol filter removed some weak precipitation while filtering out clutter and noise, as shown by the black circle in Fig. 23(b). The MsDR filter preserved the sidelobe clutter caused by GC, as shown in Fig. 23(c). In this test, the method that combined CMD and GMAP had little effect on clutter mitigation. However, the proposed method kept precipitation while suppressing almost all clutter and noise.

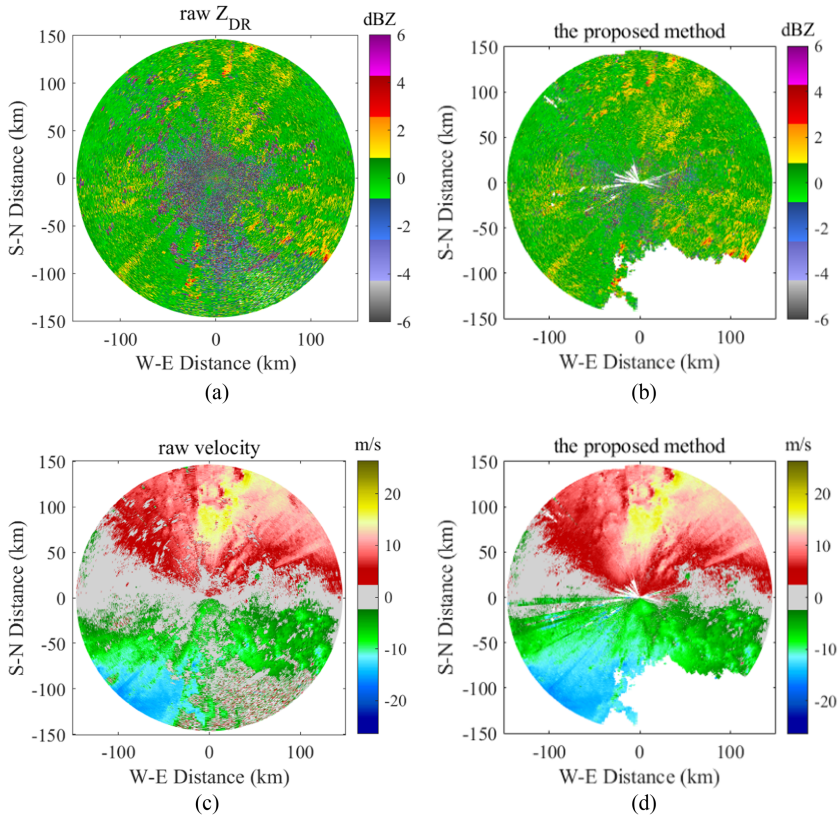

Fig. 21. PPI comparison results of Z_{DR} and $\bar{v}$ processing performance. (a) Raw Z_{DR}. (b) Z_{DR} after the proposed method processing. (c) Raw velocity. (d) Velocity after the proposed method processing.

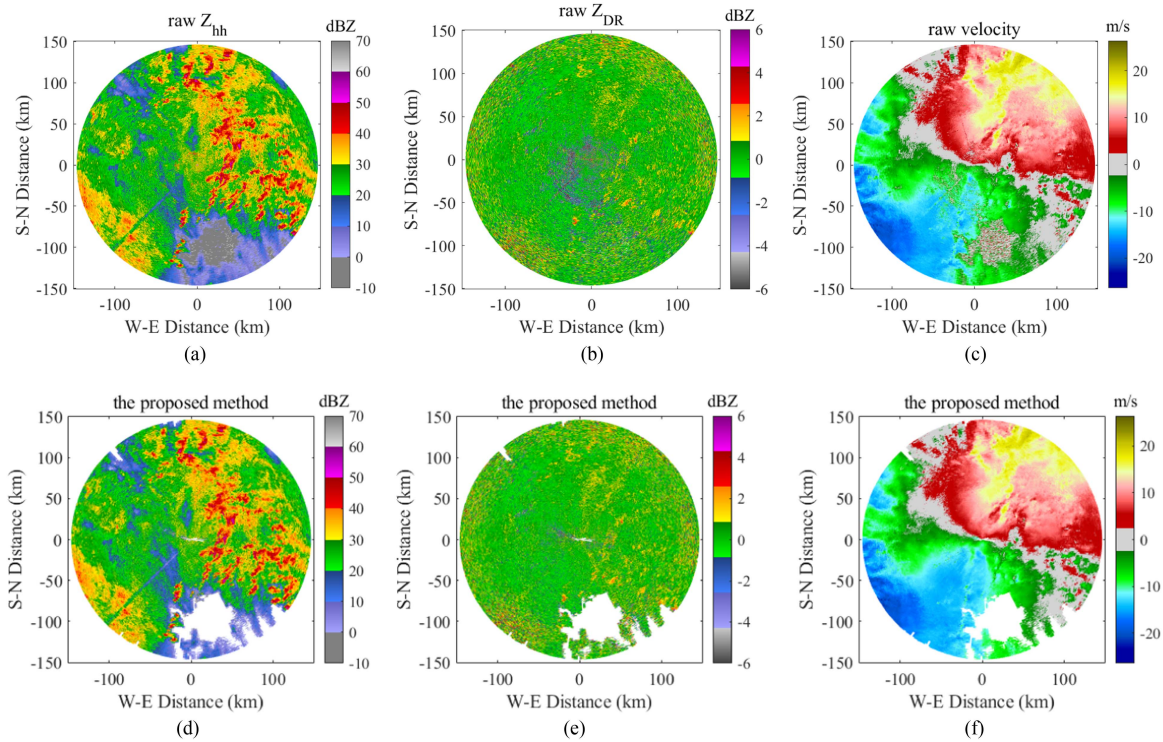

Fig. 22. PPI comparison results of Z_{hh}, Z_{DR}, and $\bar{v}$ processing performance. Data were collected by the Guangzhou radar at 5:30 on May 20, 2016, at an elevation angle of 1.5°. (a) Raw Z_{hh}. (b) Raw Z_{DR}. (c) Raw velocity. (d) Z_{hh} after the proposed method processing. (e) Z_{DR} after applying the proposed method. (f) Velocity after the proposed method processing.

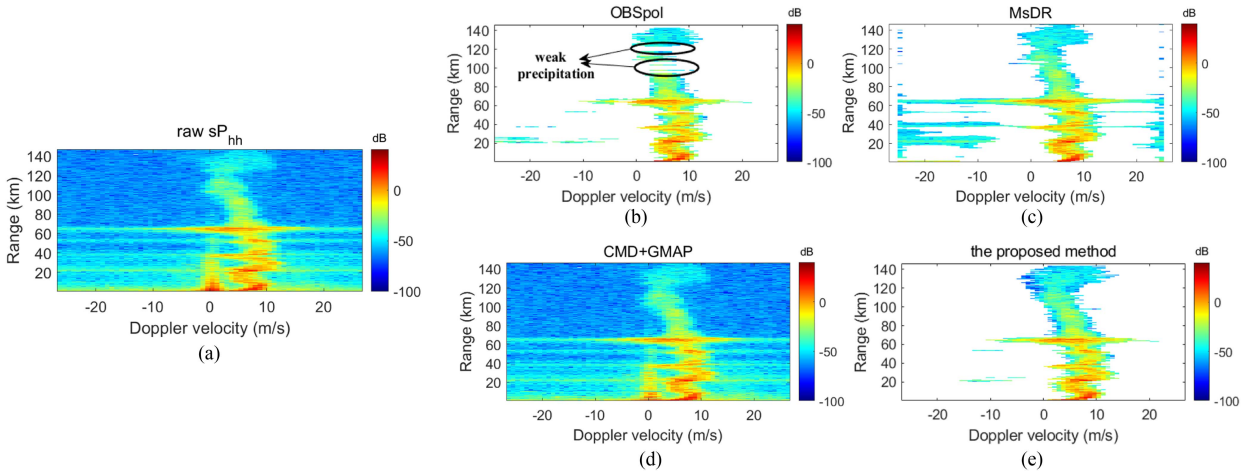

Fig. 23. Qualitative performance comparison results of the OBSpol filter, the MsDR filter, the CMD + GMAP method, and the proposed method. The RD spectrogram denotes the spectrogram corresponding to the data of Ray 90; data were collected by the Guangzhou radar at 5:31 on May 20, 2016. (a) Raw spectrogram. (b) OBSpol-filtered spectrogram. (c) MsDR-filtered spectrogram. (d) Spectrogram after applying the method that combined CMD with GMAP. (e) Spectrogram after the proposed method processing.

VI. Conclusion

This study proposes a spectral polarization method to mitigate GC and noise for polarimetric Doppler weather radar. Taking advantage of the spectral polarimetric feature and the RD continuity of precipitation, the proposed method is implemented on the RD spectrogram to mitigate clutter and noise. The proposed method includes two stages: 1) clutter filtering and 2) precipitation recovery. The filtering stage can cause precipitation loss, leading to discontinuity of precipitation. To address this problem, the weather window is estimated using the continuity of spectral moments in precipitation recovery, and then, the precipitation window is applied to the raw power spectrum to obtain precipitation.

The proposed method integrates clutter detection, filter, and precipitation recovery. Specifically designed for GC and noise suppression in the polarimetric Doppler weather radar, it is particularly suitable for radars without cross-polar measurements, which is a common configuration for operational weather radars. The proposed method can not only remove noise and GC but also recover precipitation overlapped with GC.

The performance of the proposed method is compared with three other methods. Compared with the MsDR and OBSpol filters, which tend to retain a certain amount of clutter and remove the contaminated precipitation when clutter overlaps with precipitation, the proposed method is more effective in precipitation preservation. This is due to the precipitation recovery technique adopted in the proposed algorithm design. Compared with the method that combines CMD with GMAP, which can reduce a significant amount of GC power, the proposed method has better performance in GC mitigation as it is not constrained by the assumption that the shape of the GC is approximately Gaussian.

References

[1] R. J. Doviak et al. *Doppler radar and weather observations*, New York, NY, USA: Courier Corporation, 2006.

[2] R. J. Doviak, V. Bringi, and A. Ryzhkov, "Considerations for polarimetric upgrades to operational WSR-880D radars," *J. Atmospheric Ocean. Technol.*, vol. 17, no. 3, pp. 257–278, 2000.

[3] H. Chen and V. Chandrasekar, "The quantitative precipitation estimation system for Dallas–Fort Worth (DFW) urban remote sensing network," *J. Hydrol.*, vol. 531, pp. 259–271, 2015.

[4] H. Chen, V. Chandrasekar, and R. Bechini, "An improved dual-polarization radar rainfall algorithm (DROPS2.0): Application in NASA IFloodS field campaign," *J. Hydrometeorol.*, vol. 18, no. 4, pp. 917–937, 2017.

[5] D. Rezacova, Z. Sokol, and P. Pesice, "A radar-based verification of precipitation forecast for local convective storms," *Atmospheric Res.*, vol. 83, no. 2/4, pp. 211–224, 2007.

[6] H. T. L. Huong and A. Pathirana, "Urbanization and climate change impacts on future urban flooding in Can Tho City, Vietnam," *Hydrol. Earth Syst. Sci.*, vol. 17, no. 1, pp. 379–394, 2013.

[7] J. Yin, P. Hoogeboom, C. Unal, and H. Russchenberg, "Radio frequency interference characterization and mitigation for polarimetric weather radar: A study case," *IEEE Trans. Geosci. Remote Sens.*, vol. 60, pp. 1–16, 2021.

[8] J. Yin, C. Unal, and H. Russchenberg, "Object-orientated filter design in spectral domain for polarimetric weather radar," *IEEE Trans. Geosci. Remote Sens.*, vol. 57, no. 5, pp. 2725–2740, May 2019.

[9] G. Zhang, *Weather Radar Polarimetry*. Boca Raton, FL, USA: CRC Press, 2016.

[10] A. V. Ryzhkov and D. S. Zrnic, "Polarimetric rainfall estimation in the presence of anomalous propagation," *J. Atmospheric Ocean. Technol.*, vol. 15, no. 6, pp. 1320–1330, 1998.

[11] J. B. Billingsley, "Low Angle Radar Land Clutter: Measurements and Empirical Models," 2002. [Online]. Available: https://api.semanticscholar.org/CorpusID:126665781

[12] J. C. Hubbert, M. Dixon, S. Ellis, and G. Meymaris, "Weather radar ground clutter. Part I: Identification, modeling, and simulation," *J. Atmospheric Ocean. Technol.*, vol. 26, no. 7, pp. 1165–1180, 2009.

[13] J. C. Hubbert, M. Dixon, and S. M. Ellis, "Weather radar ground clutter. Part II: Real-time identification and filtering," *J. Atmospheric Ocean. Technol.*, vol. 26, no. 7, pp. 1181–1197, 2009.

[14] Q. Cao, G. Zhang, R. D. Palmer, M. Knight, R. May, and R. J. Stafford, "Spectrum-time estimation and processing (STEP) for improving weather radar data quality," *IEEE Trans. Geosci. Remote Sens.*, vol. 50, no. 11, pp. 4670–4683, Nov. 2012.

[15] Y. Li, G. Zhang, R. J. Doviak, L. Lei, and Q. Cao, "A new approach to detect ground clutter mixed with weather signals," *IEEE Trans. Geosci. Remote Sens.*, vol. 51, no. 4, pp. 2373–2387, Apr. 2013.

[16] M. H. Golbon-Haghighi, G. Zhang, and R. J. Doviak, "Ground clutter detection for weather radar using phase fluctuation index," *IEEE Trans. Geosci. Remote Sens.*, vol. 57, no. 5, pp. 2889–2895, May 2019.

[17] M. H. Golbon-Haghighi and G. Zhang, "Detection of ground clutter for dual-polarization weather radar using a novel 3D discriminant function," *J. Atmospheric Ocean. Technol.*, vol. 36, no. 7, pp. 1285–1296, 2019.

[18] Y. Li, G. Zhang, R. J. Doviak, and D. S. SaxionSaxion, "Scan-to-Scan correlation of weather radar signals to identify ground clutter," *IEEE Geosci. Remote Sens. Lett.*, vol. 10, no. 4, pp. 855–859, Jul. 2013.
[19] R. J. Doviak, Y. Li, and G. Zhang, "Ground clutter detection using the statistical properties of signals received with a polarimetric radar," *IEEE Trans. Signal Process.*, vol. 62, no. 3, pp. 597–606, Feb. 2014.
[20] M. H. G. Haghighi, G. Zhang, Y. Li, and R. J. Doviak, "Detection of ground clutter from weather radar using a dual-polarization and dual-scan method," *Atmosphere*, vol. 7, no. 6, p. 83, 2016.
[21] N. Li, Z. Wang, K. Sun, Z. Chu, L. Leng, and X. Lv, "A quality control method of ground-based weather radar data based on statistics," *IEEE Trans. Geosci. Remote Sens.*, vol. 56, no. 4, pp. 2211–2219, Apr. 2018.
[22] S. Quan, Y. Qin, D. Xiang, W. Wang, and X. Wang, "Polarimetric decomposition-based unified manmade target scattering characterization with mathematical programming strategies," *IEEE Trans. Geosci. Remote Sens.*, vol. 60, 2022, Art. no. 5203718.
[23] S. Quan, T. Zhang, W. Wang, G. Kuang, X. Wang, and B. Zeng, "Exploring fine polarimetric decomposition technique for built-up area monitoring," *IEEE Trans. Geosci. Remote Sens.*, vol. 61, 2023, Art. no. 5204719.
[24] C. Unal, "Spectral polarimetric radar clutter suppression to enhance atmospheric echoes," *J. Atmospheric Ocean. Technol.*, vol. 26, pp. 1781–1797, 2009.
[25] J. Yin, C. Unal, and H. Russchenberg, "Narrow-band clutter mitigation in spectral polarimetric weather radar," *IEEE Trans. Geosci. Remote Sens.*, vol. 55, no. 8, pp. 4655–4667, Aug. 2017.
[26] J. Yin, H. Chen, Y. Li, and X. Wang, "Clutter mitigation based on spectral depolarization ratio for dual-polarization weather radars," *IEEE J. Sel. Topics Appl. Earth Observ. Remote Sens.*, vol. 14, pp. 6131–6145, 2021.
[27] A. D. Siggia and R. E. Passarelli, "Gaussian model adaptive processing (GMAP) for improved ground clutter cancellation and moment calculation," in *Proc. Eur. Conf. Radar Meteorol. Hydrol.*, vol. 2, pp. 421–424, 2004.
[28] J. Y. N. Cho, "Signal processing algorithms for the terminal Doppler weather radar: Build 2," 2010.
[29] D. A. Warde and S. M. Torres, "The autocorrelation spectral density for Doppler-weather-radar signal analysis," *IEEE Trans. Geosci. Remote Sens.*, vol. 52, no. 1, pp. 508–518, Jan. 2014.
[30] J. C. Hubbert, G. Meymaris, U. Romatschke, and M. Dixon, "Improving signal statistics using a regression ground clutter filter. Part I: Theory and simulations," *J. Atmospheric Ocean. Technol.*, vol. 38, 2021.
[31] J. Yin, M. Schleiss, and X. Wang, "Clutter-contaminated signal recovery in spectral domain for polarimetric weather radar," *IEEE Geosci. Remote Sens. Lett.*, vol. 19, 2022, Art. no. 3504505.
[32] F. Nai, S. Torres, and R. Palmer, "On the mitigation of wind turbine clutter for weather radars using range-Doppler spectral processing," *IET Radar, Sonar, Navigation*, vol. 7, no. 2, pp. 178–190, 2013.
[33] C. Chen, C. M. H. Unal, and A. C. P. O. Nijhuis, "Jensen–Shannon distance-based filter and unsupervised evaluation metrics for polarimetric weather radar processing," *IEEE Trans. Geosci. Remote Sens.*, vol. 60, 2022, Art. no. 5117018.
[34] I. R. Ivić, "Effects of phase coding on Doppler spectra in PPAR weather radar," *IEEE Trans. Geosci. Remote Sens.*, vol. 56, no. 4, pp. 2043–2065, Apr. 2018.

Mengyun An was born in 1997. She received the B.E. degree from Central South University, Changsha, China, in 2020. She is currently working toward the Ph.D. degree in information and communication engineering with the College of Electronic Science, National University of Defense Technology, Changsha.

Her research interest includes radar signal processing.

Jiapeng Yin received the B.Sc. degree in information engineering from the National University of Defense Technology (NUDT), Changsha, China, in 2012, and the Ph.D. degree in atmospheric remote sensing from the Delft University of Technology, Delft, The Netherlands, in 2019.

He is currently an Associate Professor with the College of Electronic Science and Technology, NUDT. His research interests include radar polarimetry, polarimetric weather radar, radar signal processing, and radar calibration.

Jiankai Huang was born in 1994. He received the B.E. degree from the Beijing Institute of Technology, Beijing, China, in 2018, and the M.S. degree from the College of Electronic Science and Engineering, National University of Defense Technology, Changsha, China, in 2020. He is currently working toward the Ph.D. degree with the College of Electronic Science, National University of Defense Technology, Changsha.

His research interest includes radar signal processing.

Xue Tan received the B.S. and M.S. degrees in electrical engineering from the Chengdu University Information Technology, Chengdu, China, in 2009 and 2013, respectively.

He is currently a Senior Engineer with CEC JinJiang Information Industry Co., Ltd., Chengdu. His research interests include weather radar signal processing and data quality.

Yongzhen Li received the B.S. and Ph.D. degrees in electronic engineering from the National University of Defense Technology, Changsha, China, in 1999 and 2004, respectively.

He is currently a Professor with the College of Electronic Science and Technology, National University of Defense Technology. His research interests include radar signal processing, radar polarimetry, and target recognition.